Re-interpreting the Oxbridge stransverse mass variable M_{T2} in general cases

Rakhi Mahbubani,[a] **Konstantin T. Matchev**[b] **and Myeonghun Park**[a,1]

[a] *CERN Physics Department, Theory Division,*
CH-1211 Geneva 23, Switzerland.

[b] *Physics Department, University of Florida,*
Gainesville, FL 32611, U.S.A.

E-mail: rakhi@cern.ch, matchev@phys.ufl.edu, Myeonghun.Park@cern.ch

ABSTRACT: We extend the range of possible applications of M_{T2} type analyses to decay chains with multiple invisible particles, as well as to asymmetric event topologies with different parent and/or different children particles. We advocate two possible approaches. In the first, we introduce suitably defined $3+1$-dimensional analogues of the M_{T2} variable, which take into account all relevant on-shell kinematic constraints in a given event topology. The second approach utilizes the conventional M_{T2} variable, but its kinematic endpoint is suitably reinterpreted on a case by case basis, depending on the specific event topology at hand. We provide the general prescription for this reinterpretation, including the formulas relating the measured M_{T2} endpoint (as a function of the test masses of all the invisible particles) to the underlying physical mass spectrum. We also provide analytical formulas for the shape of the differential distribution of the doubly projected $M_{T2_\perp}$ variable for the ten possible event topologies with one visible particle and up to two invisible particles per decay chain. We illustrate our results with the example of leptonic chargino decays $\tilde{\chi}^+ \to \ell^+ \nu \tilde{\chi}^0$ in supersymmetry.

KEYWORDS: Supersymmetry Phenomenology, Hadronic Colliders

ARXIV EPRINT: 1212.1720

---

[1]Corresponding author.

Contents

1 Introduction

The Large Hadron Collider (LHC) at CERN is continuing its quest for new physics Beyond the Standard Model (BSM). Among the multitude of possible BSM scenarios, models with neutral and stable WIMPs (weakly interacting massive particles) are of particular interest. First, such models are greatly motivated by the dark matter problem, as WIMPs are suitable dark matter candidates. Second, the initial BSM searches at the LHC have already placed stringent limits on heavy resonances which decay visibly and can be fully reconstructed. In contrast, the limits on parent particles which decay *semi-invisibly* (to a collection of visible SM particles and one or more WIMPs) are much weaker. First, the background issue in these analyses is more complicated: since the parent cannot be fully reconstructed, the search is not a mere "bump hunt", where the background can be simply subtracted from the side-bands. Second, the symmetry which protects the lifetime of the WIMP dark matter candidate typically requires that the new particles are multiply produced, leading to lower production cross-sections (as opposed to single production). In
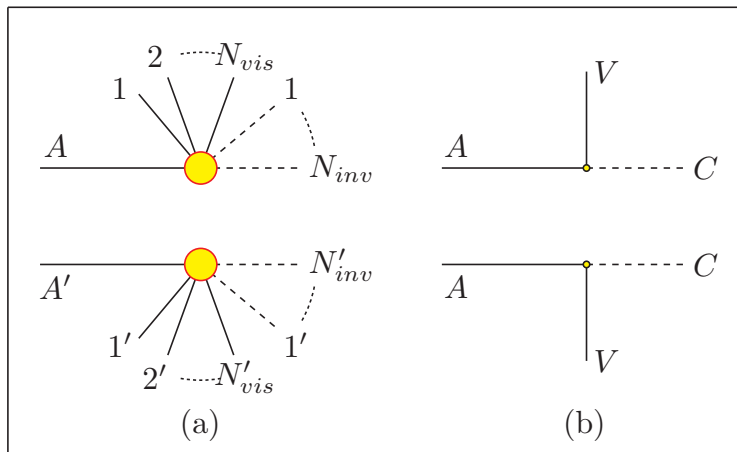
Figure 1. (a) The generic event topology for the pair production of two parent particles A and A'. Particle A (A') decays to a set of N_{vis} (N'_{vis}) particles which are visible in the detector and a set of N_{inv} (N'_{inv}) invisible particles. The invisible particles are not necessarily limited to SM neutrinos, and can have arbitrary masses. (b) The simplified event topology typically used in M_{T2} studies. Each V is either a single SM particle, or an effective composite visible particle which is constructed from the corresponding visible particles in figure (a). The decay chain for each parent A terminates in a single invisible particle C.

the simplest and most popular models, the new symmetry is a $\mathcal{Z}_2$ parity, which implies that the new particles are pair produced, as illustrated in figure 1.

Figure 1(a) depicts the generic event topology in a typical SUSY-like missing energy event. Two parent particles A and A' are produced, and each one decays to a certain number of visible particles (denoted by solid lines), and a certain number of invisible particles (denoted by dashed lines). At this point, the diagram in figure 1(a) is meant to represent the most general case: for example, the number of visible particles (N_{vis} and N'_{vis}), as well as the number of invisible particles (N_{inv} and N'_{inv}) in each parent decay chain is completely arbitrary. Furthermore, the invisible particles are not necessarily limited to SM neutrinos, but may include (several species of) WIMPs with different masses. Most importantly, no assumption has been made regarding the actual decay topology of the parents, and the yellow-shaded circles are simply placeholders for the actual $1 \to N_{vis} + N_{inv}$ and $1 \to N'_{vis} + N'_{inv}$ Feynman diagrams responsible for the parent decays in the figure.

The kinematic analysis of events of this type is rather challenging. There is a lot of missing (or a priori unknown) information: the number of invisible particles N_{inv} and N'_{inv}, the momenta (and masses) of the invisible particles, the total invariant mass and longitudinal momentum of the parent system (A, A'), and the event topologies hiding behind the yellow-shaded circles in figure 1(a). These problems have inspired a lot of previous work in the literature on new methods for measuring the masses of the parents and the invisible daughters under these circumstances (for a recent review, see [1]). Among the different options existing in the literature, the *invariant mass* variables appear to be both useful and theoretically motivated [2]. Being Lorentz-invariant, they are insensitive to the a

priori unknown longitudinal boost of the (A, A') system. A special subset of invariant mass variables which also shares this property, is given by the *transverse* invariant mass variables, among which the Oxbridge stransverse mass M_{T2} [3, 4] is a well-known example directly applicable to figure 1(a). It has been featured in analyses performed by the Tevatron and LHC experimental collaborations CDF, D0, CMS and ATLAS [5–9].

In the original proposal [3], the "Oxbridge" M_{T2} variable was applied to the case of direct slepton production, corresponding to the simple event topology shown in figure 1(b), which is a special case of the more general figure 1(a). In figure 1(b), two identical parents (A) are produced, and each one subsequently decays via a two-body decay to a single visible SM particle V and a single invisible child particle C. In spite of its simplicity, the event topology of figure 1(b) covers a number of interesting physics cases, e.g. slepton production [3, 10], squark production [11–13], chargino production [14, 15], etc. At the same time, the M_{T2} concept is very powerful, and can be usefully applied to situations that are more general than the simple example in figure 1(b).

So let us first review the different directions in which one could generalize figure 1(b). Some of the following options (a-b) have already been considered in the literature, and we only mention them here for completeness. The remaining possibilities (c-f), however, have attracted significantly less attention in the literature, and will be the main focus of this paper.

(a) In figure 1(b) there is only one visible particle in each decay chain. In the language of figure 1(a), this implies the assumption $N_{vis} = N'_{vis} = 1$. At the same type, a typical BSM model like supersymmetry exhibits much longer decay chains, with several visible particles on each side of the event. This case can be easily handled with the conventional M_{T2} approach — one just needs to think of each V as a collection of visible particles with some net four-momentum P^μ, which is measured in the detector. Early work along these lines [16–18] led to the discovery of the M_{T2} "kink" in the endpoint $M_{T2}^{\max}$ when considered as a function of the unknown test[1] mass $\tilde{M}_C$ for the child particle:

$$\left(\frac{dM_{T2}^{\max}(\tilde{M}_C)}{d\tilde{M}_C} \right)_{\tilde{M}_C = M_C(1-\epsilon)} \neq \left(\frac{dM_{T2}^{\max}(\tilde{M}_C)}{d\tilde{M}_C} \right)_{\tilde{M}_C = M_C(1+\epsilon)} . \qquad (1.1)$$

The kink in eq. (1.1) is an interesting and unique property of the M_{T2} variable, allowing to measure simultaneously (at least as a matter of principle) the true mass M_C of the invisible dark matter candidate C at the end of the decay chain *and* the true mass M_A of the parent particle initiating the decay chain. What makes the appearance of the kink possible is the fact that the invariant mass M_V of the visible collection of particles V is not constant, but varies from event to event: $M_V^2 = P^\mu P_\mu \neq const$.

(b) Another possible generalization is to consider that the parent particles A are produced *inclusively*, either in association with jets from initial state radiation, or in the decays

---

[1]Following the notation of [19], test input masses for invisible particles will be denoted by a tilde.

of other, even heavier, new particles. In either case, one again finds an M_{T2} kink in eq. (1.1) at the true mass of the daughter particle C [18, 19]. The kink persists even if the decay chain is extremely short ($N_{vis} = N'_{vis} = 1$) and $M_V = const$. This is because the origin of the kink is now different — it is due to the net transverse momentum of the parent system (A, A).

(c) Another limiting assumption in figure 1(b) is that the two missing particles C at the end of each decay chain are the same (or at least have a common mass M_C). This assumption, however, can be easily relaxed — one simply needs to allow for two independent mass inputs $\tilde{M}_{C_1}$ and $\tilde{M}_{C_2}$ in the calculation of M_{T2} [20]. The resulting "asymmetric" M_{T2} variable inherits all the desired properties of the conventional M_{T2}. In particular, the "kink" in eq. (1.1) in the function $M_{T2}^{\max}(\tilde{M}_C)$ is generalized to a kinky "crease" in the surface defined by the function $M_{T2}^{\max}(\tilde{M}_{C_1}, \tilde{M}_{C_2})$ [20, 21]. While this all sounds very straightforward, one should keep in mind that the original public codes [22, 23] for calculating the M_{T2} variable cannot be used in this case, since the assumption $\tilde{M}_{C_1} = \tilde{M}_{C_2}$ is already hardwired.[2]

(d) The other assumption in figure 1(b) is that the two parent particles are the same (or at least have a common mass M_A). In principle, this can also be handled rather easily. If the parents are different, but the children are the same, then one of the decay chains must have additional visible particles which are not present on the other side. Then, one possibility is to try to identify the extra particles and remove them from consideration, thus reducing the effective event topology back to figure 1(b) [25]. An alternative strategy is to consider the full event, but allow for different parent masses $\tilde{M}_{A_1}$ and $\tilde{M}_{A_2}$ and then use $M_{T2}^{\max}$ to construct the function $\tilde{M}_C(\tilde{M}_{A_1}, \tilde{M}_{A_2})$ [21].

(e) Another assumption of figure 1(b) is that there is a *single* invisible particle in each decay chain, i.e. that $N_{inv} = N'_{inv} = 1$. Again, there is no compelling reason for this restriction in light of generic BSM models. First, a $\mathcal{Z}_N$ parity restricts the number of dark matter candidates in each decay chain only modulo N. Second, a $\mathcal{Z}_3$ parity can lead to $N_{inv} = 2$ as easily as $N_{inv} = 1$ [26]. Finally, and most importantly, we already know that SM neutrinos exist and behave like invisible particles at colliders. The decay chains in figure 1 can easily[3] contain SM neutrino particles, which would contribute to the total invisible particle count N_{inv} [27]. Under those circumstances, one needs to generalize the M_{T2} variable to account for the extra invisible particles, and define corresponding variables M_{T3}, M_{T4}, etc. [4], where the numerical subscript indicates the number of invisible particles N_{inv}. In doing so, however, one faces the following fundamental problem. Recall that the most useful property of the original M_{T2} variable was that its endpoint $M_{T2}^{\max}$ *equals* the true parent mass M_A when the test child mass $\tilde{M}_C$ coincides with the true child mass M_C:

$$M_{T2}^{\max}(\tilde{M}_{C_i} = M_{C_i}) = M_A. \tag{1.2}$$

---

[2]However, see [24] for an update to [23].

[3]The standard example is the chargino decay in supersymmetry $\tilde{\chi}_1^\pm \to \ell^\pm \nu \tilde{\chi}_1^0$, which gives *two* invisible particles — a neutrino ν and a neutralino $\tilde{\chi}_1^0$.

However, as we shall explicitly see below in section 3, this property depends crucially on the assumption that there aren't any additional invisible particles in the game. In reality, whenever the collection of particles V in figure 1(b) contains other invisible particles χ *in addition to* the invisible child particle C, and there are intermediate on-shell resonances in the cascade decay chain, the bound of eq. (1.2) is not necessarily saturated, and one can only write

$$M_{T2}^{\max}(M_\chi + M_C) \leq M_A. \tag{1.3}$$

The inequality applies even when the true masses M_χ and M_C are being used. The same holds for the new "generalized" variables M_{T3}, M_{T4}, etc. from [4]. In fact, these generalized variables are simply related to the asymmetric M_{T2} variable [20] as follows[4]

$$M_{T3}(\tilde{M}_{C_1}, \tilde{M}_{\chi_1}; \tilde{M}_{C_2}) = M_{T2}(\tilde{M}_{C_1} + \tilde{M}_{\chi_1}, \tilde{M}_{C_2}), \tag{1.4}$$

$$M_{T4}(\tilde{M}_{C_1}, \tilde{M}_{\chi_1}; \tilde{M}_{C_2}, \tilde{M}_{\chi_2}) = M_{T2}(\tilde{M}_{C_1} + \tilde{M}_{\chi_1}, \tilde{M}_{C_2} + \tilde{M}_{\chi_2}), \tag{1.5}$$

and so on. Therefore, the endpoints of M_{T3}, M_{T4}, etc. are also *not* guaranteed to provide a saturated bound like eq. (1.2) and instead the best one can do with them is to put a lower limit on M_A as in eq. (1.3). One of the main goals of this paper, therefore, will be to address the problem of multiple invisible particles and propose how to recover *saturated* bounds of the type in eq. (1.2).

(f) The final issue is inherently related to the previous point: once we allow for multiple invisible particles ($N_{inv} > 1$) in the decay chains, we must also address the question of the correct event topology. In other words, we must ask the question, which Feynman diagram is hiding behind the yellow-shaded placeholder in figure 1(a). Most studies in the literature already assume that the correct event topology is known and rarely discuss what happens when this assumption is incorrect [28–32]. Consider, for example, the simplest possible case of one visible particle on each side ($N_{vis} = N'_{vis} = 1$) and then let us allow up to two invisible particles in a given decay chain ($N_{inv} \leq 2$ and $N'_{inv} \leq 2$). Even for this simple case, there are 10 possible decay topologies which are explicitly shown in figure 2(a-j). Furthermore, since one cannot be absolutely sure that the two visible particles originated from opposite decay chains, in principle one should also contemplate event topologies with $N_{vis} = 2$ and $N'_{vis} = 0$, and two such examples are shown in figure 2(k-l).

The main goal of this paper is to illustrate the application of the Oxbridge M_{T2} variable in the more general situations described in (c-f) above. We shall be particularly concerned with the issue (e) of multiple invisible particles and the related problem (f) of the unknown decay topology. It is quite difficult to construct a kinematic variable (or more generally, some kind of object) which would single out the correct event topology. An initial attempt in this direction was made in ref. [33] which considered the decay of a *single* resonance A

---

[4]Here and below our notation is that the additional invisible particle χ_i appears in the same decay chain as the invisible child particle C_i. See figure 2 for explicit examples.
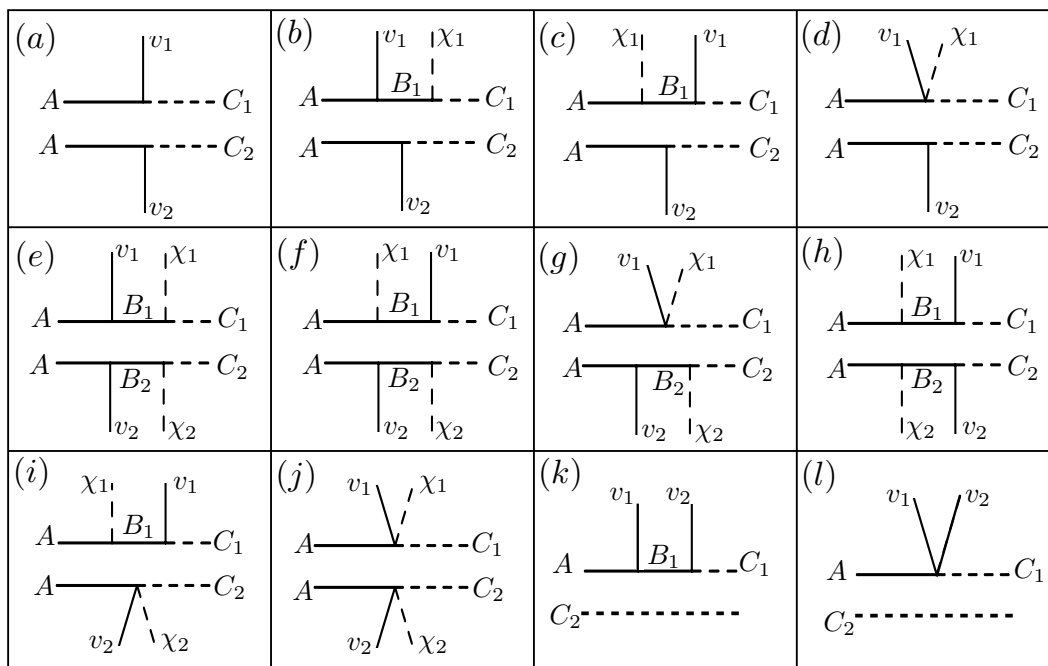
Figure 2. Possible event topologies with two visible particles v_1 and v_2 in the final state and up to 2 invisible particles $\{C_i, \chi_i\}$ per decay chain. B_1 and B_2 are intermediate on-shell resonances: $M_A > M_{B_i} > M_{C_i}$.

(as opposed to pair production as in figure 1) and studied the invariant mass distribution M_V of the visible decay products. It was suggested that there exists a correlation between the peak, the curvature at the peak, and the endpoint of the M_V distribution, which in favorable scenarios can be used to infer the decay topology and the number of invisibles N_{inv}. However, this method requires $N_{vis} \geq 2$ and cannot be used to discriminate the topologies of figure 2(a-j), for which $N_{vis} = 1$ and $M_V = M_{v_i} = const$.

It appears, therefore, that we need to study event topologies on a case by case basis, i.e., assume in turn each one of the event topologies from figure 2, then test for consistency with the data. Note that the event topologies differ from each other in two aspects:

1. The number of invisible particles N_{inv}. For example, the diagrams in figure 2(a,k,l) have $N_{inv} = N'_{inv} = 1$, the diagrams in figure 2(e-j) have $N_{inv} = N'_{inv} = 2$, while the diagrams in figure 2(b-d) have $N_{inv} = 2$ and $N'_{inv} = 1$.

2. Different number of intermediate on-shell resonances B_i. For example, the diagrams in figure 2(a,d,j,l) have no intermediate resonances, the diagrams in figure 2(b,c,g,i,k) have one, while the diagrams in figure 2(e,f,h) have two.

As already discussed earlier, both of these effects jeopardize the conventional M_{T2} approach, and some modifications are required. In principle, there are two possible solutions. The first, presented in section 2, is to modify the conventional M_{T2} definition on a case by case basis — depending on the assumed event topology. The new definitions will use the

appropriate number of invisible particles, and will also take into account the relevant on-shell kinematic constraints — one constraint for each intermediate resonance B_i. Because the mass shell constraints are $3 + 1$-dimensional relations, this approach does not use the transverse M_{T2} variable per se, but the alternative $3+1$ dimensional invariant mass variable M_2 from [2], supplemented with the appropriate mass-shell constraints (see also [34, 35] and the analogous constrained variables M_{2C} and M_{3C}). The advantage of this approach is that we do not have to change the *interpretation* of the corresponding kinematic endpoint $M_2^{\max}$ — it still provides a *saturated* bound on the parent mass in terms of the masses of the invisible daughter particles, similarly to eq. (1.2).

On the other hand, from a practical standpoint, the constrained M_2 method has a certain disadvantage: one has to define a new M_2 variable for each assumed event topology. In the majority of the cases, those variables are *not* equivalent to the conventional M_{T2}, and therefore cannot be calculated with the existing M_{T2} codes [22, 23]. Since analytical formulas are also unavailable, one would have to write a separate code for each variable. The mass-shell constraints represent an additional complication, since most likely they will have to be solved analytically first [36–38]. This is why in section 3 we present an alternative approach whereby one keeps the original definition of M_{T2} (thus being able to recycle the existing numerical codes), and instead modifies the *interpretation* of the kinematic endpoint $M_{T2}^{\max}$ on a case by case basis. The basic idea was raised in [39], where it was applied to the M_{CT} variable [40] in the example of chargino decay. Here we show that one can apply a similar treatment to the M_{T2} kinematic endpoints, and we also provide the recipe for a general event topology.

In section 4 and section 5 we extend our method to the case of different children particles (C_1 and C_2) and different parent particles (A_1 and A_2), respectively. Finally, in section 6 we study the impact of the number of invisible particles N_{inv} on the shape of the $M_{T2_\perp}$ distribution [41]. The technique was originally proposed in [27], which focused on the shape of the M_{T2} variable. Here we prefer to consider the doubly projected version $M_{T2_\perp}$, which is less sensitive to extraneous factors like spin correlations, the underlying partonic CM energy $\sqrt{s}$, etc. [42]. Thus our analysis completes the generalization of M_{T2} along the lines (c-f) discussed above. Since the directions (a) and (b) have already been discussed extensively in the literature, for the sake of clarity and simplicity, throughout the paper we shall use the simplest assumption $N_{vis} = N'_{vis} = 1$ and we shall introduce upstream P_T (i.e., transverse momentum for the parent system (A, A)) only as necessary.

2　Maximally constrained invariant mass variables

In this section we revisit the event topologies from figure 2 and for each one define the appropriate invariant mass variable which provides the maximal bound on the parent mass M_A [2].

The event topology of figure 2(a). This is the classic M_{T2} event topology from figure 1(b), so the relevant variable is simply M_{T2} [3] (or its asymmetric version if the children have different masses [20]). For future reference, it is convenient to introduce here

the $3 + 1$-dimensional version of M_{T2}, denoted simply as M_2,[5] which will make it very easy to incorporate additional mass-shell constraints later on.

M_2 is defined on a case by case basis, following the general recipe outlined in [2]. The particles in the final state are divided into two groups[6] (hence the subscript "2" on M_2), one for each parent. Then, the larger of the two parent masses is minimized over the momenta of the invisible particles. The minimization is performed subject to all existing kinematic constraints and assumptions. The measurement of the missing transverse momentum $\vec{\slashed{P}}_T$ always provides one constraint on the net sum of the invisible transverse momenta, and another constraint is due to the assumption that the parents have equal masses (see discussion of item (d) in the Introduction).

In the case of the diagram in figure 2(a), there are no further constraints, and we get

$$M_{2(a)}^2(\tilde{M}_{C_1}; \tilde{M}_{C_2}) = \min_{P_{C_1}, P_{C_2}} \left\{ (P_{v_1} + P_{C_1})^2 \right\} \tag{2.1}$$

$$(P_{v_1} + P_{C_1})^2 = (P_{v_2} + P_{C_2})^2$$

$$P_{C_1}^2 = \tilde{M}_{C_1}^2$$

$$P_{C_2}^2 = \tilde{M}_{C_2}^2$$

$$\vec{P}_{TC_1} + \vec{P}_{TC_2} = \vec{\slashed{P}}_T$$

Upon performing the minimization over the longitudinal momenta P_{zC_1} and P_{zC_2}, one finds that eq. (2.1) is equivalent [2, 34] to the usual M_{T2} when the children's masses are taken to be the same

$$M_{2(a)}(\tilde{M}_C; \tilde{M}_C) = M_{T2}(\tilde{M}_C), \tag{2.2}$$

or to the asymmetric M_{T2} [20]

$$M_{2(a)}(\tilde{M}_{C_1}; \tilde{M}_{C_2}) = M_{T2}(\tilde{M}_{C_1}, \tilde{M}_{C_2}), \tag{2.3}$$

if the children's masses are kept different.

The event topology of figure 2(b). Proceeding as before, for the diagram in figure 2(b) we get

$$M_{2(b)}^2(\tilde{M}_{\chi_1}, \tilde{M}_{C_1}; \tilde{M}_{C_2}) = \min_{P_{\chi_1}, P_{C_1}, P_{C_2}} \left\{ (P_{v_1} + P_{\chi_1} + P_{C_1})^2 \right\}. \tag{2.4}$$

$$(P_{v_1} + P_{\chi_1} + P_{C_1})^2 = (P_{v_2} + P_{C_2})^2$$

$$P_{\chi_1}^2 = \tilde{M}_{\chi_1}^2$$

$$P_{C_1}^2 = \tilde{M}_{C_1}^2$$

$$P_{C_2}^2 = \tilde{M}_{C_2}^2$$

$$(P_{\chi_1} + P_{C_1})^2 = M_{B_1}^2$$

$$\vec{P}_{T\chi_1} + \vec{P}_{TC_1} + \vec{P}_{TC_2} = \vec{\slashed{P}}_T$$

---

[5]Not to be confused with the wino mass parameter in supersymmetry.

[6]The division into two groups is motivated by the two parent hypothesis. If we do not make this assumption and instead treat the event as a whole, we are led to the global inclusive variable $\sqrt{\hat{s}}_{\min}$ [43, 44], which in the language of [2] is denoted as M_1.

With $P_{B_1} \equiv P_{\chi_1} + P_{C_1}$, this can be equivalently written as

$$M^2_{2(b)}(\tilde{M}_{\chi_1}, \tilde{M}_{C_1}; \tilde{M}_{C_2}) = \min_{P_{B_1}, P_{C_2}} \left\{ (P_{v_1} + P_{B_1})^2 \right\}. \tag{2.5}$$

$$(P_{v_1} + P_{B_1})^2 = (P_{v_2} + P_{C_2})^2$$
$$P^2_{B_1} = M^2_{B_1}$$
$$P^2_{C_2} = \tilde{M}^2_{C_2}$$
$$\vec{P}_{TB_1} + \vec{P}_{TC_2} = \vec{\not{P}}_T$$

From here, comparing to eq. (2.1) and taking into account eq. (2.3), it follows that

$$M_{2(b)}(\tilde{M}_{\chi_1}, \tilde{M}_{C_1}; \tilde{M}_{C_2}) = M_{2(a)}(M_{B_1}; \tilde{M}_{C_2}) = M_{T2}(M_{B_1}, \tilde{M}_{C_2}). \tag{2.6}$$

As expected, the kinematics of figure 2(b) is described by the asymmetric M_{T2} variable [20], with the intermediate invisible resonance B_1 treated effectively as a final state invisible particle.

The event topology of figure 2(c). We get

$$M^2_{2(c)}(\tilde{M}_{\chi_1}, \tilde{M}_{C_1}; \tilde{M}_{C_2}) = \min_{P_{\chi_1}, P_{C_1}, P_{C_2}} \left\{ (P_{v_1} + P_{\chi_1} + P_{C_1})^2 \right\}. \tag{2.7}$$

$$(P_{v_1} + P_{\chi_1} + P_{C_1})^2 = (P_{v_2} + P_{C_2})^2$$
$$P^2_{\chi_1} = \tilde{M}^2_{\chi_1}$$
$$P^2_{C_1} = \tilde{M}^2_{C_1}$$
$$P^2_{C_2} = \tilde{M}^2_{C_2}$$
$$(P_{v_1} + P_{C_1})^2 = M^2_{B_1}$$
$$\vec{P}_{T\chi_1} + \vec{P}_{TC_1} + \vec{P}_{TC_2} = \vec{\not{P}}_T$$

This variable is new — it cannot be related to existing versions of the M_{T2} variables as in eqs. (2.3), (2.6).

The event topology of figure 2(d). Here there are no mass-shell constraints and we have

$$M^2_{2(d)}(\tilde{M}_{\chi_1}, \tilde{M}_{C_1}; \tilde{M}_{C_2}) = \min_{P_{\chi_1}, P_{C_1}, P_{C_2}} \left\{ (P_{v_1} + P_{\chi_1} + P_{C_1})^2 \right\}. \tag{2.8}$$

$$(P_{v_1} + P_{\chi_1} + P_{C_1})^2 = (P_{v_2} + P_{C_2})^2$$
$$P^2_{\chi_1} = \tilde{M}^2_{\chi_1}$$
$$P^2_{C_1} = \tilde{M}^2_{C_1}$$
$$P^2_{C_2} = \tilde{M}^2_{C_2}$$
$$\vec{P}_{T\chi_1} + \vec{P}_{TC_1} + \vec{P}_{TC_2} = \vec{\not{P}}_T$$

It is easy to show that the minimization in eq. (2.8) selects the collinear momentum configuration [2, 43]

$$\vec{P}_{\chi_1} = \frac{\tilde{M}_{\chi_1}}{\tilde{M}_{C_1}} \vec{P}_{C_1} \tag{2.9}$$

and eq. (2.8) can be rewritten as

$$M_{2(d)}^2(\tilde{M}_{\chi_1}, \tilde{M}_{C_1}; \tilde{M}_{C_2}) = \min_{P_{\Psi_1}, P_{C_2}} \left\{ (P_{v_1} + P_{\Psi_1})^2 \right\}. \tag{2.10}$$

$$(P_{v_1} + P_{\Psi_1})^2 = (P_{v_2} + P_{C_2})^2$$

$$P_{\Psi_1}^2 = (\tilde{M}_{\chi_1} + \tilde{M}_{C_1})^2$$

$$P_{C_2}^2 = \tilde{M}_{C_2}^2$$

$$\vec{P}_{T\Psi_1} + \vec{P}_{TC_2} = \vec{\slashed{P}}_T$$

in terms of an effective composite invisible particle Ψ_1 with mass

$$\tilde{M}_{\Psi_1} \equiv \tilde{M}_{\chi_1} + \tilde{M}_{C_1} \tag{2.11}$$

and 3-momentum

$$\vec{P}_{\Psi_1} \equiv \vec{P}_{\chi_1} + \vec{P}_{C_1} = \frac{\tilde{M}_{\Psi_1}}{\tilde{M}_{C_1}} \vec{P}_{C_1} = \frac{\tilde{M}_{\Psi_1}}{\tilde{M}_{\chi_1}} \vec{P}_{\chi_1}. \tag{2.12}$$

Comparing to eq. (2.1), we recognize this as the asymmetric M_{T2} variable in eq. (2.3) [20]

$$M_{2(d)}(\tilde{M}_{\chi_1}, \tilde{M}_{C_1}; \tilde{M}_{C_2}) = M_{2(a)}(\tilde{M}_{\chi_1} + \tilde{M}_{C_1}; \tilde{M}_{C_2}) = M_{T2}(\tilde{M}_{\chi_1} + \tilde{M}_{C_1}, \tilde{M}_{C_2}). \tag{2.13}$$

The event topology of figure 2(e). This is our first example with *four* invisible particles:

$$M_{2(e)}^2(\tilde{M}_{\chi_1}, \tilde{M}_{C_1}; \tilde{M}_{\chi_2}, \tilde{M}_{C_2}) = \min_{P_{\chi_1}, P_{C_1}, P_{\chi_2}, P_{C_2}} \left\{ (P_{v_1} + P_{\chi_1} + P_{C_1})^2 \right\}. \tag{2.14}$$

$$(P_{v_1} + P_{\chi_1} + P_{C_1})^2 = (P_{v_2} + P_{\chi_2} + P_{C_2})^2$$

$$P_{\chi_1}^2 = \tilde{M}_{\chi_1}^2$$

$$P_{C_1}^2 = \tilde{M}_{C_1}^2$$

$$P_{\chi_2}^2 = \tilde{M}_{\chi_2}^2$$

$$P_{C_2}^2 = \tilde{M}_{C_2}^2$$

$$(P_{\chi_1} + P_{C_1})^2 = M_{B_1}^2$$

$$(P_{\chi_2} + P_{C_2})^2 = M_{B_2}^2$$

$$\vec{P}_{T\chi_1} + \vec{P}_{TC_1} + \vec{P}_{T\chi_2} + \vec{P}_{TC_2} = \vec{\slashed{P}}_T$$

By introducing $P_{B_i} \equiv P_{\chi_i} + P_{C_i}, (i = 1, 2)$, this can be equivalently rewritten as

$$M_{2(e)}^2(\tilde{M}_{\chi_1}, \tilde{M}_{C_1}; \tilde{M}_{\chi_2}, \tilde{M}_{C_2}) = \min_{P_{B_1}, P_{B_2}} \left\{ (P_{v_1} + P_{B_1})^2 \right\} \tag{2.15}$$

$$(P_{v_1} + P_{B_1})^2 = (P_{v_2} + P_{B_2})^2$$

$$P_{B_1}^2 = M_{B_1}^2$$

$$P_{B_2}^2 = M_{B_2}^2$$

$$\vec{P}_{TB_1} + \vec{P}_{TB_2} = \vec{\slashed{P}}_T$$

and therefore is again reduced to the asymmetric M_{T2} [20]

$$M_{2(e)}(\tilde{M}_{\chi_1}, \tilde{M}_{C_1}; \tilde{M}_{\chi_2}, \tilde{M}_{C_2}) = M_{2(a)}(M_{B_1}; M_{B_2}) = M_{T2}(M_{B_1}, M_{B_2}). \tag{2.16}$$

Notice that $M_{2(e)}$ does *not* depend on the test masses $\tilde{M}_{\chi_1}, \tilde{M}_{C_1}, \tilde{M}_{\chi_1}$ and $\tilde{M}_{C_2}$. In fact, the two invisible decays $B_i \to \chi_i + C_i, (i = 1, 2)$, have no observable consequences.

The event topology of figure 2(f). This is similar to the previous case, except the order in which particles χ_1 and v_1 appear in the decay chain is reversed

$$M_{2(f)}^2(\tilde{M}_{\chi_1}, \tilde{M}_{C_1}; \tilde{M}_{\chi_2}, \tilde{M}_{C_2}) = \min_{P_{\chi_1}, P_{C_1}, P_{\chi_2}, P_{C_2}} \left\{ (P_{v_1} + P_{\chi_1} + P_{C_1})^2 \right\}. \quad (2.17)$$

$$(P_{v_1} + P_{\chi_1} + P_{C_1})^2 = (P_{v_2} + P_{\chi_2} + P_{C_2})^2$$
$$P_{\chi_1}^2 = \tilde{M}_{\chi_1}^2$$
$$P_{C_1}^2 = \tilde{M}_{C_1}^2$$
$$P_{\chi_2}^2 = \tilde{M}_{\chi_2}^2$$
$$P_{C_2}^2 = \tilde{M}_{C_2}^2$$
$$(P_{v_1} + P_{C_1})^2 = M_{B_1}^2$$
$$(P_{\chi_2} + P_{C_2})^2 = M_{B_2}^2$$
$$\vec{P}_{T\chi_1} + \vec{P}_{TC_1} + \vec{P}_{T\chi_2} + \vec{P}_{TC_2} = \vec{P}\!\!\!/_T$$

Once again, the B_2 mass shell constraint causes the inputs $\tilde{M}_{\chi_2}$ and $\tilde{M}_{C_2}$ to drop out and we get

$$M_{2(f)}^2(\tilde{M}_{\chi_1}, \tilde{M}_{C_1}; \tilde{M}_{\chi_2}, \tilde{M}_{C_2}) = \min_{P_{\chi_1}, P_{C_1}, P_{B_2}} \left\{ (P_{v_1} + P_{\chi_1} + P_{C_1})^2 \right\}. \quad (2.18)$$

$$(P_{v_1} + P_{\chi_1} + P_{C_1})^2 = (P_{v_2} + P_{B_2})^2$$
$$P_{\chi_1}^2 = \tilde{M}_{\chi_1}^2$$
$$P_{C_1}^2 = \tilde{M}_{C_1}^2$$
$$P_{B_2}^2 = M_{B_2}^2$$
$$(P_{v_1} + P_{C_1})^2 = M_{B_1}^2$$
$$\vec{P}_{T\chi_1} + \vec{P}_{TC_1} + \vec{P}_{TB_2} = \vec{P}\!\!\!/_T$$

This variable is also different from M_{T2}, but is related to $M_{2(c)}$:

$$M_{2(f)}(\tilde{M}_{\chi_1}, \tilde{M}_{C_1}; \tilde{M}_{\chi_2}, \tilde{M}_{C_2}) = M_{2(c)}(\tilde{M}_{\chi_1}, \tilde{M}_{C_1}; \tilde{M}_{B_2}). \quad (2.19)$$

The event topology of figure 2(g). This case is similar to figure 2(e), but the B_1 mass shell constraint is removed:

$$M_{2(g)}^2(\tilde{M}_{\chi_1}, \tilde{M}_{C_1}; \tilde{M}_{\chi_2}, \tilde{M}_{C_2}) = \min_{P_{\chi_1}, P_{C_1}, P_{\chi_2}, P_{C_2}} \left\{ (P_{v_1} + P_{\chi_1} + P_{C_1})^2 \right\}. \quad (2.20)$$

$$(P_{v_1} + P_{\chi_1} + P_{C_1})^2 = (P_{v_2} + P_{\chi_2} + P_{C_2})^2$$
$$P_{\chi_1}^2 = \tilde{M}_{\chi_1}^2$$
$$P_{C_1}^2 = \tilde{M}_{C_1}^2$$
$$P_{\chi_2}^2 = \tilde{M}_{\chi_2}^2$$
$$P_{C_2}^2 = \tilde{M}_{C_2}^2$$
$$(P_{\chi_2} + P_{C_2})^2 = M_{B_2}^2$$
$$\vec{P}_{T\chi_1} + \vec{P}_{TC_1} + \vec{P}_{T\chi_2} + \vec{P}_{TC_2} = \vec{P}\!\!\!/_T$$

Introducing the effective particle Ψ as in eqs. (2.11), (2.12), we get

$$M_{2(g)}^2(\tilde{M}_{\chi_1}, \tilde{M}_{C_1}; \tilde{M}_{\chi_2}, \tilde{M}_{C_2}) = \min_{P_{\Psi_1}, P_{B_2}} \left\{ (P_{v_1} + P_{\Psi_1})^2 \right\}. \qquad (2.21)$$

$$(P_{v_1} + P_{\Psi_1})^2 = (P_{v_2} + P_{B_2})^2$$
$$P_{\Psi_1}^2 = (\tilde{M}_{\chi_1} + \tilde{M}_{C_1})^2$$
$$P_{B_2}^2 = M_{B_2}^2$$
$$\vec{P}_{T\Psi_1} + \vec{P}_{TB_2} = \vec{\not{P}}_T$$

and therefore

$$M_{2(g)}(\tilde{M}_{\chi_1}, \tilde{M}_{C_1}; \tilde{M}_{\chi_2}, \tilde{M}_{C_2}) = M_{2(a)}(\tilde{M}_{\chi_1} + \tilde{M}_{C_1}; M_{B_2}) = M_{T2}(\tilde{M}_{\chi_1} + \tilde{M}_{C_1}, M_{B_2}). \quad (2.22)$$

The event topology of figure 2(h). This is another new and non-trivial case:

$$M_{2(h)}^2(\tilde{M}_{\chi_1}, \tilde{M}_{C_1}; \tilde{M}_{\chi_2}, \tilde{M}_{C_2}) = \min_{P_{\chi_1}, P_{C_1}, P_{\chi_2}, P_{C_2}} \left\{ (P_{v_1} + P_{\chi_1} + P_{C_1})^2 \right\}. \qquad (2.23)$$

$$(P_{v_1} + P_{\chi_1} + P_{C_1})^2 = (P_{v_2} + P_{\chi_2} + P_{C_2})^2$$
$$P_{\chi_1}^2 = \tilde{M}_{\chi_1}^2$$
$$P_{C_1}^2 = \tilde{M}_{C_1}^2$$
$$P_{\chi_2}^2 = \tilde{M}_{\chi_2}^2$$
$$P_{C_2}^2 = \tilde{M}_{C_2}^2$$
$$(P_{v_1} + P_{C_1})^2 = M_{B_1}^2$$
$$(P_{v_2} + P_{C_2})^2 = M_{B_2}^2$$
$$\vec{P}_{T\chi_1} + \vec{P}_{TC_1} + \vec{P}_{T\chi_2} + \vec{P}_{TC_2} = \vec{\not{P}}_T$$

The variable $M_{2(h)}$ cannot be reduced to one of the previous variables and would have to be evaluated separately.

An interesting variation of the $M_{2(h)}$ variable arises in the symmetric case when the intermediate on-shell particles B_1 and B_2 are the same, with $M_{B_1} = M_{B_2}$. Then, one can replace the two mass shell constraints for B_1 and B_2 with the requirement that the B_1 and B_2 masses are equal, but without specifying the actual numerical value:

$$M_{2(h)}^2(\tilde{M}_{\chi_1}, \tilde{M}_{C_1}; \tilde{M}_{\chi_2}, \tilde{M}_{C_2}) = \min_{P_{\chi_1}, P_{C_1}, P_{\chi_2}, P_{C_2}} \left\{ (P_{v_1} + P_{\chi_1} + P_{C_1})^2 \right\}. \qquad (2.24)$$

$$(P_{v_1} + P_{\chi_1} + P_{C_1})^2 = (P_{v_2} + P_{\chi_2} + P_{C_2})^2$$
$$P_{\chi_1}^2 = \tilde{M}_{\chi_1}^2$$
$$P_{C_1}^2 = \tilde{M}_{C_1}^2$$
$$P_{\chi_2}^2 = \tilde{M}_{\chi_2}^2$$
$$P_{C_2}^2 = \tilde{M}_{C_2}^2$$
$$(P_{v_1} + P_{C_1})^2 = (P_{v_2} + P_{C_2})^2$$
$$\vec{P}_{T\chi_1} + \vec{P}_{TC_1} + \vec{P}_{T\chi_2} + \vec{P}_{TC_2} = \vec{\not{P}}_T$$

The advantage of this approach is that one does not need to know the value of $M_{B_1} = M_{B_2}$ beforehand.

The event topology of figure 2(i). This is similar to the previous case, except the B_2 mass shell constraint is absent:

$$M_{2(i)}^2(\tilde{M}_{\chi_1}, \tilde{M}_{C_1}; \tilde{M}_{\chi_2}, \tilde{M}_{C_2}) = \min_{P_{\chi_1}, P_{C_1}, P_{\chi_2}, P_{C_2}} \left\{ (P_{v_1} + P_{\chi_1} + P_{C_1})^2 \right\}. \qquad (2.25)$$

$$(P_{v_1} + P_{\chi_1} + P_{C_1})^2 = (P_{v_2} + P_{\chi_2} + P_{C_2})^2$$
$$P_{\chi_1}^2 = \tilde{M}_{\chi_1}^2$$
$$P_{C_1}^2 = \tilde{M}_{C_1}^2$$
$$P_{\chi_2}^2 = \tilde{M}_{\chi_2}^2$$
$$P_{C_2}^2 = \tilde{M}_{C_2}^2$$
$$(P_{v_1} + P_{C_1})^2 = M_{B_1}^2$$
$$\vec{P}_{T\chi_1} + \vec{P}_{TC_1} + \vec{P}_{T\chi_2} + \vec{P}_{TC_2} = \vec{\slashed{P}}_T$$

With the help of the effective invisible particle Ψ, this can be again simplified:

$$M_{2(i)}^2(\tilde{M}_{\chi_1}, \tilde{M}_{C_1}; \tilde{M}_{\chi_2}, \tilde{M}_{C_2}) = \min_{P_{\chi_1}, P_{C_1}, P_{\Psi_2}} \left\{ (P_{v_1} + P_{\chi_1} + P_{C_1})^2 \right\}. \qquad (2.26)$$

$$(P_{v_1} + P_{\chi_1} + P_{C_1})^2 = (P_{v_2} + P_{\Psi_2})^2$$
$$P_{\chi_1}^2 = \tilde{M}_{\chi_1}^2$$
$$P_{C_1}^2 = \tilde{M}_{C_1}^2$$
$$P_{\Psi_2}^2 = (\tilde{M}_{\chi_2} + \tilde{M}_{C_2})^2$$
$$(P_{v_1} + P_{C_1})^2 = M_{B_1}^2$$
$$\vec{P}_{T\chi_1} + \vec{P}_{TC_1} + \vec{P}_{T\Psi_2} = \vec{\slashed{P}}_T$$

Comparing to eq. (2.7), we see that this variable is related to $M_{2(c)}$:

$$M_{2(i)}(\tilde{M}_{\chi_1}, \tilde{M}_{C_1}; \tilde{M}_{\chi_2}, \tilde{M}_{C_2}) = M_{2(c)}(\tilde{M}_{\chi_1}, \tilde{M}_{C_1}; \tilde{M}_{\chi_2} + \tilde{M}_{C_2}). \qquad (2.27)$$

The event topology of figure 2(j). Here there are no mass shell constraints and we have

$$M_{2(j)}^2(\tilde{M}_{\chi_1}, \tilde{M}_{C_1}; \tilde{M}_{\chi_2}, \tilde{M}_{C_2}) = \min_{P_{\chi_1}, P_{C_1}, P_{\chi_2}, P_{C_2}} \left\{ (P_{v_1} + P_{\chi_1} + P_{C_1})^2 \right\}. \qquad (2.28)$$

$$(P_{v_1} + P_{\chi_1} + P_{C_1})^2 = (P_{v_2} + P_{\chi_2} + P_{C_2})^2$$
$$P_{\chi_1}^2 = \tilde{M}_{\chi_1}^2$$
$$P_{C_1}^2 = \tilde{M}_{C_1}^2$$
$$P_{\chi_2}^2 = \tilde{M}_{\chi_2}^2$$
$$P_{C_2}^2 = \tilde{M}_{C_2}^2$$
$$\vec{P}_{T\chi_1} + \vec{P}_{TC_1} + \vec{P}_{T\chi_2} + \vec{P}_{TC_2} = \vec{\slashed{P}}_T$$

Introducing two effective invisible particles Ψ_1 and Ψ_2, this reduces to

$$M_{2(j)}^2(\tilde{M}_{\chi_1}, \tilde{M}_{C_1}; \tilde{M}_{\chi_2}, \tilde{M}_{C_2}) = \min_{P_{\Psi_1}, P_{\Psi_2}} \left\{ (P_{v_1} + P_{\Psi_1})^2 \right\}. \qquad (2.29)$$

$$(P_{v_1} + P_{\Psi_1})^2 = (P_{v_2} + P_{\Psi_2})^2$$
$$P_{\Psi_1}^2 = (\tilde{M}_{\chi_1} + \tilde{M}_{C_1})^2$$
$$P_{\Psi_2}^2 = (\tilde{M}_{\chi_2} + \tilde{M}_{C_2})^2$$
$$\vec{P}_{T\Psi_1} + \vec{P}_{T\Psi_2} = \vec{\not{P}}_T$$

Comparing to eq. (2.1), we see that

$$
\begin{aligned}
M_{2(j)}(\tilde{M}_{\chi_1}, \tilde{M}_{C_1}; \tilde{M}_{\chi_2}, \tilde{M}_{C_2}) &= M_{2(a)}(\tilde{M}_{\chi_1} + \tilde{M}_{C_1}; \tilde{M}_{\chi_2} + \tilde{M}_{C_2}) \\
&= M_{T2}(\tilde{M}_{\chi_1} + \tilde{M}_{C_1}, \tilde{M}_{\chi_2} + \tilde{M}_{C_2}).
\end{aligned}
\tag{2.30}
$$

In conclusion of this section, let us summarize its main points. We considered the ten event topologies in figure 2(a-j) and defined the corresponding maximally constrained invariant mass variables, which fell into three categories.

- The variable $M_{2(a)}$ and its cousins $M_{2(b)}$, $M_{2(d)}$, $M_{2(e)}$, $M_{2(g)}$, and $M_{2(j)}$, all of which can be computed in terms of the asymmetric M_{T2}:

$$
\begin{aligned}
M_{2(b)}(\tilde{M}_{\chi_1}, \tilde{M}_{C_1}; \tilde{M}_{C_2}) &= M_{2(a)}(M_{B_1}; \tilde{M}_{C_2}) \\
&= M_{T2}(M_{B_1}, \tilde{M}_{C_2}) \\
M_{2(d)}(\tilde{M}_{\chi_1}, \tilde{M}_{C_1}; \tilde{M}_{C_2}) &= M_{2(a)}(\tilde{M}_{\chi_1} + \tilde{M}_{C_1}; \tilde{M}_{C_2}) \\
&= M_{T2}(\tilde{M}_{\chi_1} + \tilde{M}_{C_1}, \tilde{M}_{C_2}) \\
M_{2(e)}(\tilde{M}_{\chi_1}, \tilde{M}_{C_1}; \tilde{M}_{\chi_2}, \tilde{M}_{C_2}) &= M_{2(a)}(M_{B_1}; M_{B_2}) \\
&= M_{T2}(M_{B_1}, M_{B_2}) \\
M_{2(g)}(\tilde{M}_{\chi_1}, \tilde{M}_{C_1}; \tilde{M}_{\chi_2}, \tilde{M}_{C_2}) &= M_{2(a)}(\tilde{M}_{\chi_1} + \tilde{M}_{C_1}; M_{B_2}) \\
&= M_{T2}(\tilde{M}_{\chi_1} + \tilde{M}_{C_1}, M_{B_2}) \\
M_{2(j)}(\tilde{M}_{\chi_1}, \tilde{M}_{C_1}; \tilde{M}_{\chi_2}, \tilde{M}_{C_2}) &= M_{2(a)}(\tilde{M}_{\chi_1} + \tilde{M}_{C_1}; \tilde{M}_{\chi_2} + \tilde{M}_{C_2}) \\
&= M_{T2}(\tilde{M}_{\chi_1} + \tilde{M}_{C_1}, \tilde{M}_{\chi_2} + \tilde{M}_{C_2})
\end{aligned}
$$

- The variable $M_{2(c)}$ and its friends $M_{2(f)}$ and $M_{2(i)}$:

$$
\begin{aligned}
M_{2(f)}(\tilde{M}_{\chi_1}, \tilde{M}_{C_1}; \tilde{M}_{\chi_2}, \tilde{M}_{C_2}) &= M_{2(c)}(\tilde{M}_{\chi_1}, \tilde{M}_{C_1}; \tilde{M}_{B_2}) \\
M_{2(i)}(\tilde{M}_{\chi_1}, \tilde{M}_{C_1}; \tilde{M}_{\chi_2}, \tilde{M}_{C_2}) &= M_{2(c)}(\tilde{M}_{\chi_1}, \tilde{M}_{C_1}; \tilde{M}_{\chi_2} + \tilde{M}_{C_2})
\end{aligned}
$$

- The variable $M_{2(h)}$.

The advantage of these maximally constrained invariant mass variables is that their endpoints provide saturated bounds on the parent mass M_A. In other words, we recover the main feature in eq. (1.2) of M_{T2} which was lost due to the presence of the mass shell constraints. More specifically, when we choose the test masses $\tilde{M}_{\chi_i}$ and $\tilde{M}_{C_i}$ to be the true ones (denoted without a tilde), the corresponding M_2 kinematic endpoint gives the parent mass M_A:

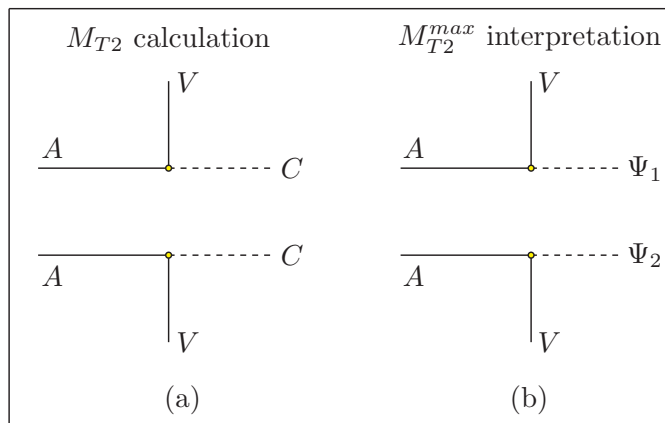$$M_{2(\ldots)}^{\max}(M_{\chi_i}, M_{C_i}) = M_A. \tag{2.31}$$

Figure 3. The effective topology used for (a) the calculation of the M_{T2} variable and (b) the interpretation of its endpoint $M_{T2}^{\max}$ in the different cases from figure 2. In panel (b), Ψ_1 and Ψ_2 are effective particles whose masses are calculated in terms of the physical masses M_A, M_B, M_C and M_χ according to the rules in figure 4.

Here the subscript $(\ldots)$ stands for the event topology specifier: $(a), (b), \ldots (j)$. This also reveals the main problem with the maximally constrained variables $M_{2(\ldots)}$ — while we recovered a saturated bound in eq. (2.31), we only managed to do so at the cost of introducing a separate M_2 variable for each event topology. Furthermore, in many cases, these variables cannot be calculated with the existing public codes. This motivates an alternative, more practical approach, which will be the subject of the next section.

3 Effective event topology and reinterpretation of the kinematic endpoint of the usual M_{T2} variable

3.1 General setup

In this section, we revisit the 10 event topologies in figure 2(a-j) and insist that we analyze all of them by means of the conventional M_{T2} variable, which is computable by the public codes. In other words, for the *calculation* of the M_{T2} variable, we will disregard any differences between the diagrams in figure 2(a-j) and instead pretend that the events arise from the classic M_{T2} event topology shown in figure 3(a): two parents with equal masses M_A are produced, and each one subsequently undergoes a two body decay to a single visible particle V with constant mass[7] $M_V = const$ and a single invisible particle C with mass M_C. As usual, we assume that the two children particles are identical (or at the very least, that they have a common mass M_C).

Following the usual procedure, we can then build the $M_{T2}(\tilde{M}_C)$ distribution and extract its endpoint $M_{T2}^{\max}(\tilde{M}_C)$. It is only at this point that we need to worry about the actual origin of the events. In order to account for the differences between the diagrams in figure 2(a-j), we propose to *interpret* the measured endpoint $M_{T2}^{\max}(\tilde{M}_C)$ in terms of the

---

[7]For simplicity, in this paper we consider massless V particles, i.e. $M_V = 0$.
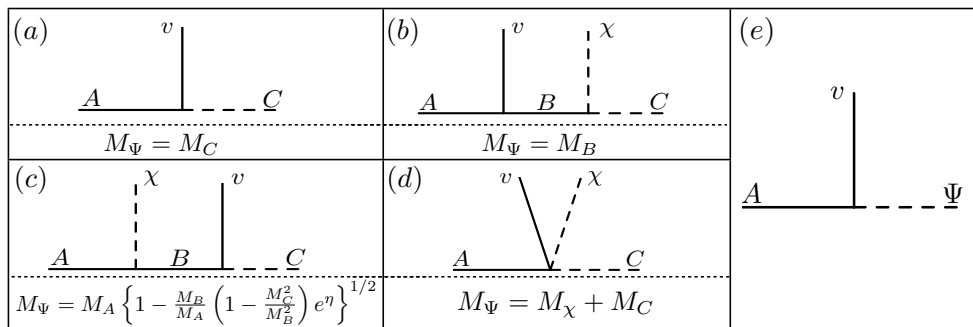
Figure 4. Equivalence diagrams for the interpretation of $M_{T2}^{\max}$ in Fig 3(b). Each decay chain (a-d) can be replaced with the effective vertex (e). The mass M_Ψ of the effective particle Ψ should be suitably chosen as shown in each panel (a-d).

effective event topology shown in figure 3(b): we still produce two identical parents, but now they decay to *effective* invisible particles Ψ_1 and Ψ_2, respectively. The interpretation of the endpoint $M_{T2}^{\max}(\tilde{M}_C)$ is still given by the usual formula [16, 17]

$$M_{T2}^{\max}(\tilde{M}_C) = \mu + \sqrt{\mu^2 + \tilde{M}_C^2}, \tag{3.1}$$

where

$$\mu \equiv \frac{M_A}{2}\left[\left(1 - \frac{M_{\Psi_1}^2}{M_A^2}\right)\left(1 - \frac{M_{\Psi_2}^2}{M_A^2}\right)\right]^{1/2}, \tag{3.2}$$

and it is only the masses M_{Ψ_1} and M_{Ψ_2} of the effective particles that would have to be calculated on a case by case basis, depending on the assumed event topology from figure 2. The effective masses $M_{\Psi_i}, (i = 1, 2)$ are in general functions of the *true* masses of the particles appearing in the corresponding event topology from figure 2. In order to derive those functions, we use the technique originally suggested in [39] for the case of the contransverse variable M_{CT}. The main idea is to consider the extreme momentum configuration which gives the maximum value $M_{T2}^{\max}$. The rules for constructing the effective mass M_Ψ for a given cascade decay chain are listed in figure 4. Most of them should be pretty intuitive, given our discussion in the previous section, where we already had to introduce an effective particle Ψ. For example, we already encountered figure 4(d) in eq. (2.11) and we also saw the replacement of figure 4(b) in eq. (2.6). Perhaps the one non-trivial example is that of figure 4(c), where the effective particle mass is formed as

$$M_{\Psi_i}(M_A, M_{B_i}, M_{C_i}, M_{\chi_i}) = M_A\left\{1 - \frac{M_{B_i}}{M_A}\left(1 - \frac{M_{C_i}^2}{M_{B_i}^2}\right)e^{\eta_i}\right\}^{1/2}, \tag{3.3}$$

where

$$\eta_i = \cosh^{-1}\left(\frac{M_A^2 + M_{B_i}^2 - M_{\chi_i}^2}{2M_A M_{B_i}}\right). \tag{3.4}$$

We present the derivation of eq. (3.3) in appendix A. When the invisible particle χ is massless ($M_\chi = 0$), the effective mass M_{Ψ_i} in eq. (3.3) reduces to

$$M_{\Psi_i}(M_A, M_{B_i}, M_{C_i}, 0) = M_{C_i}\left(\frac{M_A}{M_{B_i}}\right).$$
(3.5)

The advantage of the M_{T2} endpoint reinterpretation approach is that one never has to stray from the conventional procedure — it is only at the very last stage of the analysis that the event topology issue comes into play. The $M_{T2}^{\max}$ endpoint is always interpreted universally as in eq. (3.1), and only the parameter μ from eq. (3.2) depends on the event topology from figure 2:

$$\mu_{(a)} = \frac{M_A}{2}\sqrt{\left(1 - \frac{M_{C_1}^2}{M_A^2}\right)\left(1 - \frac{M_{C_2}^2}{M_A^2}\right)},$$
(3.6)

$$\mu_{(b)} = \frac{M_A}{2}\sqrt{\left(1 - \frac{M_{B_1}^2}{M_A^2}\right)\left(1 - \frac{M_{C_2}^2}{M_A^2}\right)},$$
(3.7)

$$\mu_{(c)} = e^{\eta_1/2}\frac{M_A}{2}\sqrt{\frac{M_{B_1}}{M_A}\left(1 - \frac{M_{C_1}^2}{M_{B_1}^2}\right)\left(1 - \frac{M_{C_2}^2}{M_A^2}\right)},$$
(3.8)

$$\mu_{(d)} = \frac{M_A}{2}\sqrt{\left(1 - \frac{(M_{C_1} + M_{\chi_1})^2}{M_A^2}\right)\left(1 - \frac{M_{C_2}^2}{M_A^2}\right)},$$
(3.9)

$$\mu_{(e)} = \frac{M_A}{2}\sqrt{\left(1 - \frac{M_{B_1}^2}{M_A^2}\right)\left(1 - \frac{M_{B_2}^2}{M_A^2}\right)},$$
(3.10)

$$\mu_{(f)} = e^{\eta_1/2}\frac{M_A}{2}\sqrt{\frac{M_{B_1}}{M_A}\left(1 - \frac{M_{C_1}^2}{M_{B_1}^2}\right)\left(1 - \frac{M_{B_2}^2}{M_A^2}\right)},$$
(3.11)

$$\mu_{(g)} = \frac{M_A}{2}\sqrt{\left(1 - \frac{(M_{C_1} + M_{\chi_1})^2}{M_A^2}\right)\left(1 - \frac{M_{B_2}^2}{M_A^2}\right)},$$
(3.12)

$$\mu_{(h)} = e^{(\eta_1+\eta_2)/2}\frac{M_A}{2}\sqrt{\frac{M_{B_1}M_{B_2}}{M_A^2}\left(1 - \frac{M_{C_1}^2}{M_{B_1}^2}\right)\left(1 - \frac{M_{C_2}^2}{M_{B_2}^2}\right)},$$
(3.13)

$$\mu_{(i)} = e^{\eta_1/2}\frac{M_A}{2}\sqrt{\frac{M_{B_1}}{M_A}\left(1 - \frac{M_{C_1}^2}{M_{B_1}^2}\right)\left(1 - \frac{(M_{C_2} + M_{\chi_2})^2}{M_A^2}\right)},$$
(3.14)

$$\mu_{(j)} = \frac{M_A}{2}\sqrt{\left(1 - \frac{(M_{C_1} + M_{\chi_1})^2}{M_A^2}\right)\left(1 - \frac{(M_{C_2} + M_{\chi_2})^2}{M_A^2}\right)},$$
(3.15)

with η_i still given by eq. (3.4).

3.2 Application to chargino decays

A well-motivated and relevant physics case illustrating the decay topologies in figure 4 is provided by the chargino decays in supersymmetry. If we identify the parent particle A with the chargino $\tilde{\chi}^+$ and the visible SM particle with a charged lepton ℓ^+, the invisible daughter particles could be: a neutralino $\tilde{\chi}^0$, a sneutrino $\tilde{\nu}$, or a SM neutrino ν. Then each of the decay chains in figure 4(a-d) can be interpreted as follows:

- The topology of figure 4(a): $A \to v + C$. This corresponds to a two-body decay of the chargino to a lepton and sneutrino: $\tilde{\chi}^+ \to \ell^+ + \tilde{\nu}$, with the sneutrino being the lightest supersymmetric particle (LSP).

- The topology of figure 4(b): $A \to v + B$, followed by $B \to \chi + C$. This is similar to the previous case, where we identify B with the sneutrino: $\tilde{\chi}^+ \to \ell^+ + \tilde{\nu}$, only this time the sneutrino decays further invisibly: $\tilde{\nu} \to \nu + \tilde{\chi}^0$.

- The topology of figure 4(c): $A \to \chi + B$, followed by $B \to v + C$. Here there are two possible examples. The first one is analogous to the sneutrino decay considered above — only this time the intermediate particle is a charged slepton $\tilde{\ell}^+$ and we get $\tilde{\chi}^+ \to \nu + \tilde{\ell}^+$, followed by $\tilde{\ell}^+ \to \ell^+ + \tilde{\chi}^0$. The invisible particle masses are identified as $M_C = M_{\tilde{\chi}^0}$ and $M_\chi = M_\nu = 0$. Another possibility is to have the chargino decay to an on-shell W boson: $\tilde{\chi}^+ \to \tilde{\chi}^0 + W^+$, followed by $W^+ \to \ell^+ + \nu$, in which case the invisible masses are $M_C = M_\nu = 0$ and $M_\chi = M_{\tilde{\chi}^0}$.

- The topology of figure 4(d): $A \to v + \chi + C$. This is realized if the chargino two-body decays are closed and it decays via a virtual slepton or W boson: $\tilde{\chi}^+ \to \ell^+ + \nu + \tilde{\chi}^0$.

By pairing up these 4 cases, we can obtain all 10 event topologies from figure 2(a-j).

As a specific scenario realizing these patterns, let us consider the Tchislepslep simplified model [45], where $M_{\tilde{\chi}^+} > M_{\tilde{\nu}_L} \simeq M_{\tilde{\ell}_L^+} > M_{\tilde{\chi}^0}$. The masses of the sneutrino and the charged slepton are taken to be equal because they belong to the same $SU(2)_W$ doublet (they are both left-handed). The two possible chargino decays are given by figure 4(b) and figure 4(c) and have equal branching fractions. The three possible ways of pairing up figure 4(b) and figure 4(c) lead to the event topologies of figure 2(e), figure 2(f) and figure 2(h):

- *Sneutrino-sneutrino.* When both charginos decay through a sneutrino as in figure 4(b), we obtain the event topology of figure 2(e) with the identifications $M_A = M_{\tilde{\chi}^+}$, $M_{B_1} = M_{B_2} = M_{\tilde{\nu}}$, $M_{C_1} = M_{C_2} = M_{\tilde{\chi}^0}$, and $M_{\chi_1} = M_{\chi_2} = M_\nu = 0$. Therefore the M_{T2} endpoint in eq. (3.1) should be interpreted with the $\mu_{(e)}$ parameter taken from eq. (3.10):

$$\mu_{(e)} \equiv \mu_{\tilde{\nu}\tilde{\nu}} = \frac{M_{\chi^+}}{2}\left(1 - \frac{M_{\tilde{\nu}}^2}{M_{\tilde{\chi}^+}^2}\right). \tag{3.16}$$

- *Slepton-sneutrino.* The hybrid pairing of figure 4(b) and figure 4(c) leads to the event topology of figure 2(f) with the identifications $M_A = M_{\tilde{\chi}^+}$, $M_{B_1} = M_{\tilde{\ell}^+}$, $M_{B_2} = M_{\tilde{\nu}}$,
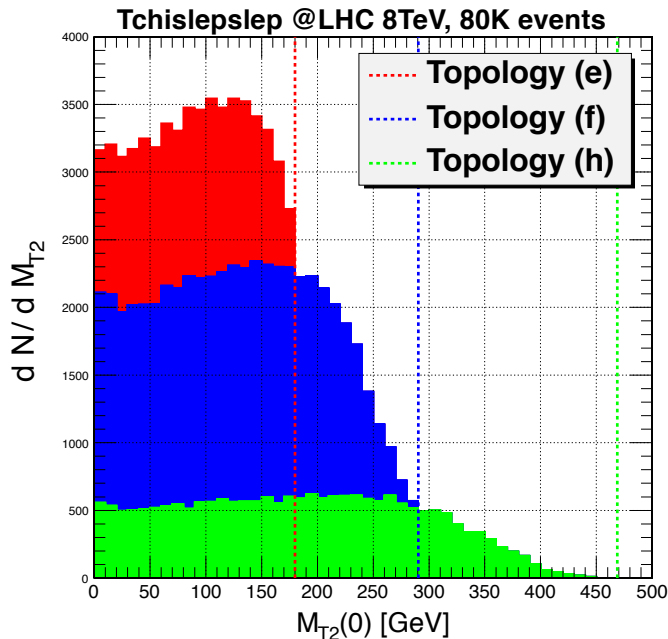
Figure 5. Distributions of the M_{T2} variable (for zero test mass $\tilde{M}_C = 0$) for the `Tchislepslep` simplified model, with $M_{\tilde{\chi}^+} = 500\,\text{GeV}$, $M_{\tilde{\nu}_L} \simeq M_{\tilde{\ell}_L^+} = 400\,\text{GeV}$ and $M_{\tilde{\chi}^0} = 100\,\text{GeV}$. The chargino branching fractions are fixed as $B(\tilde{\chi}^+ \to \ell^+ + \tilde{\nu}) = B(\tilde{\chi}^+ \to \nu + \tilde{\ell}^+) = 50\%$. Results are shown for direct chargino pair production at the LHC with 8 TeV CM energy. The vertical dashed lines mark the expected endpoints for each event topology: sneutrino-sneutrino (red), sneutrino-slepton (blue) and slepton-slepton (green).

$M_{C_1} = M_{C_2} = M_{\tilde{\chi}^0}$, and $M_{\chi_1} = M_{\chi_2} = M_\nu = 0$. The M_{T2} endpoint for such events is interpreted with $\mu_{(f)}$ from eq. (3.11):

$$\mu_{(f)} \equiv \mu_{\tilde{\ell}\tilde{\nu}} = \frac{M_{\chi^+}}{2} \sqrt{\left(1 - \frac{M_{\tilde{\chi}^0}^2}{M_{\tilde{\ell}}^2}\right)\left(1 - \frac{M_{\tilde{\nu}}^2}{M_{\tilde{\chi}^+}^2}\right)}. \tag{3.17}$$

- *Slepton-slepton.* When both charginos decay through a slepton as in figure 4(c), we obtain the event topology of figure 2(h) with the identifications $M_A = M_{\tilde{\chi}^+}$, $M_{B_1} = M_{B_2} = M_{\tilde{\ell}^+}$, $M_{C_1} = M_{C_2} = M_{\tilde{\chi}^0}$, and $M_{\chi_1} = M_{\chi_2} = M_\nu = 0$. The M_{T2} endpoint for such events is interpreted with $\mu_{(h)}$ from eq. (3.13):

$$\mu_{(h)} \equiv \mu_{\tilde{\ell}\tilde{\ell}} = \frac{M_{\chi^+}}{2}\left(1 - \frac{M_{\tilde{\chi}^0}^2}{M_{\tilde{\ell}}^2}\right). \tag{3.18}$$

The `Tchislepslep` scenario is illustrated in figure 5, where we show M_{T2} distributions from Monte Carlo simulations for direct chargino pair production, at the LHC with 8 TeV CM energy. The electroweak mass spectrum is chosen as $M_{\tilde{\chi}^+} = 500\,\text{GeV}$, $M_{\tilde{\nu}_L} \simeq M_{\tilde{\ell}_L^+} = 400\,\text{GeV}$ and $M_{\tilde{\chi}^0} = 100\,\text{GeV}$, while the chargino branching fractions are fixed as $B(\tilde{\chi}^+ \to$

$\ell^+ + \tilde{\nu}) = B(\tilde{\chi}^+ \to \nu + \tilde{\ell}^+) = 50\%$. For simplicity, we calculate M_{T2} with zero test mass $(\tilde{M}_C = 0)$, so that the endpoint formula in eq. (3.1) simplifies to

$$M_{T2}^{\max}(\tilde{M}_C = 0) = 2\mu = \begin{cases} 180 \text{ GeV for sneutrino} - \text{sneutrino events,} \\ 290 \text{ GeV for slepton} - \text{sneutrino events,} \\ 469 \text{ GeV for slepton} - \text{slepton events.} \end{cases} \quad (3.19)$$

where the μ parameter was calculated from eqs. (3.16)–(3.18), depending on the event type. In figure 5, sneutrino-sneutrino events are plotted in red, slepton-sneutrino events are plotted in blue and slepton-slepton events are plotted in green. The color-coded vertical dashed lines mark the corresponding M_{T2} endpoints expected from eqs. (3.16)–(3.19).

We conclude this section with a discussion of the `TChiww` SMS model, in which the sleptons and sneutrinos are heavy, and both charginos decay through an on-shell W boson instead (provided, of course, that $M_{\tilde{\chi}^+} > M_W + M_{\tilde{\chi}^0}$). The corresponding topology is the one from figure 2(h), where $C_i = \nu$ and $\chi_i = \tilde{\chi}^0$ is the neutralino LSP. The effective masses from eq. (3.3) are

$$M_{\Psi_1} = M_{\Psi_2} = M_{\tilde{\chi}^+} \sqrt{1 - \frac{M_W}{M_{\tilde{\chi}^+}} e^\eta}, \quad (3.20)$$

where

$$\eta = \cosh^{-1}\left(\frac{M_{\tilde{\chi}^+}^2 + M_W^2 - M_{\tilde{\chi}^0}^2}{2M_{\tilde{\chi}^+} M_W}\right). \quad (3.21)$$

Then the M_{T2} endpoint (with zero test mass $\tilde{M}_{\tilde{\chi}^0}$) is given by

$$M_{T2}^{\max}(0) = M_W\, e^\eta. \quad (3.22)$$

Finally, if the mass splitting between the chargino and the neutralino is small ($M_{\tilde{\chi}^+} - M_{\tilde{\chi}^0} < M_W$), the chargino decays as in figure 4(d). The event topology is given in figure 2(j) and the M_{T2} endpoint (again with zero test mass $\tilde{M}_{\tilde{\chi}^0}$) is

$$M_{T2}^{\max}(0) = M_{\tilde{\chi}^+}\left(1 - \frac{M_{\tilde{\chi}^0}^2}{M_{\tilde{\chi}^+}^2}\right). \quad (3.23)$$

4 Reinterpretation of the kinematic endpoint of the asymmetric M_{T2} variable

In the effective topology of figure 3(a), the test masses for the two invisible children were chosen to be the same: $\tilde{M}_C$. However, as demonstrated in [20], it is straightforward to generalize the standard M_{T2} calculation in figure 3(a) to allow for *different* test masses for the two children particles. In other words, we could use the effective diagram in figure 3(b) not only for the *interpretation* of the kinematic endpoint, but also for the actual *calculation* of the (asymmetric) M_{T2} variable itself, in terms of two *different* test masses,[8] $\tilde{M}_{\Psi_1}$ and $\tilde{M}_{\Psi_2}$ [20]:

$$M_{T2D}(\tilde{M}_{\Psi_1}, \tilde{M}_{\Psi_2}) \equiv \min_{\vec{P}_{T\Psi_1} + \vec{P}_{T\Psi_2} = \vec{\not{P}}_T} \left\{ \max\left\{ M_{TA_1}(\vec{P}_{T\Psi_1}, \tilde{M}_{\Psi_1}),\ M_{TA_2}(\vec{P}_{T\Psi_2}, \tilde{M}_{\Psi_2}) \right\} \right\}, \quad (4.1)$$

---

[8]Recall our notation that test masses always carry a tilde.

where M_{TA_i} is the transverse mass of the parent particle A_i

$$M_{TA_i}(\vec{P}_{T\Psi_i}, \tilde{M}_{\Psi_i}) \equiv \left[M_{V_i}^2 + \tilde{M}_{\Psi_i}^2 + 2\left(\sqrt{M_{V_i}^2 + \vec{P}_{TV_i}^2} \sqrt{\tilde{M}_{\Psi_i}^2 + \vec{P}_{T\Psi_i}^2} - \vec{P}_{TV_i} \cdot \vec{P}_{T\Psi_i} \right) \right]^{1/2}.$$
(4.2)

and the subscript "D" in eq. (4.1) is used to remind the reader that the asymmetric M_{T2} variable uses two different test mass inputs. In eq. (4.2), M_{V_i} and $\vec{P}_{TV_i}$ are correspondingly the invariant mass and transverse momentum of the effective visible particle V_i resulting from the decay of A_i. Similarly, $\tilde{M}_{\Psi_i}$ and $\vec{P}_{T\Psi_i}$ are the test mass and test transverse momentum of the effective invisible particle Ψ_i (see figure 3(b)). As usual, $\vec{P}_{T\Psi_1}$ and $\vec{P}_{T\Psi_2}$ are subject to the missing transverse momentum constraint, and then varied to find the minimum of the function in eq. (4.1).

When the visible particles are massless ($M_{V_i} = 0$), as we are considering here, the kinematic endpoint of M_{T2D} is given by [20]

$$M_{T2D}^{\max}(\tilde{M}_{\Psi_1}, \tilde{M}_{\Psi_2}) = \left[\left(\mu + \sqrt{\mu^2 + \tilde{M}_+^2 + \frac{\tilde{M}_-^4}{4\mu^2}} \right)^2 - \frac{\tilde{M}_-^4}{4\mu^2} \right]^{1/2},$$
(4.3)

where the parameter μ encoding the dependence on the physical masses is still given by eq. (3.2), while the two test masses enter through the combinations

$$\tilde{M}_+^2 = \frac{1}{2}\left(\tilde{M}_{\Psi_1}^2 + \tilde{M}_{\Psi_2}^2 \right),$$
(4.4)

$$\tilde{M}_-^2 = \frac{1}{2}\left| \tilde{M}_{\Psi_1}^2 - \tilde{M}_{\Psi_2}^2 \right|.$$
(4.5)

Obviously, one can always go from the asymmetric M_{T2D} variable in eq. (4.1) back to the original M_{T2} variable [3], simply by setting the two test masses to be equal:

$$M_{T2D}(\tilde{M}_\Psi, \tilde{M}_\Psi) = M_{T2}(\tilde{M}_\Psi).$$
(4.6)

Furthermore, the M_{T2D} endpoint in eq. (4.3) only allows us to measure one parameter: μ, and the same can be said about the usual M_{T2} endpoint in eq. (3.1) as well. A natural question then is whether there is any benefit at all from introducing the more complicated variable M_{T2D}. We see two motivations for considering M_{T2D}:

- In the context of manifestly asymmetric event topologies like the ones shown in figure 2(b), figure 2(c), figure 2(d), figure 2(f), figure 2(g) and figure 2(i), the language of M_{T2D} is more appropriate because the masses of the *effective* invisible particles Ψ_1 and Ψ_2 are different, even if the masses of the particles C_1 and C_2 at the end of the decay chains are the same.

- More importantly, by considering the asymmetric M_{T2D} variable, one could in principle find not just one constraint among the three unknown parameters M_A, M_{Ψ_1} and M_{Ψ_2}, but the actual values of all three parameters themselves [20, 21]. To this end, one needs to consider events in which the parent AA system recoils against upstream

objects (from initial state radiation or prior decays) with a net upstream transverse momentum U_T. One then measures the endpoint in eq. (4.3) and compares the results in different U_T bins. In general, the results for the M_{T2D} endpoint will depend on the value of U_T. However, when the test masses $\tilde{M}_{\Psi_i}$ are equal to the corresponding *true values* M_{Ψ_i}, the U_T dependence disappears and $M_{T2D}^{\max}$ becomes independent of the upstream momentum [20]:

$$\frac{\partial M_{T2D}^{\max}}{\partial U_T}\bigg|_{\tilde{M}_{\Psi_i}=M_{\Psi_i}} = 0. \tag{4.7}$$

The true location of the invisible masses M_{Ψ_i} is often also revealed as the crossing point of several creases in the two-dimensional hyper-surface defined by the function $M_{T2D}^{\max}(\tilde{M}_{\Psi_1}, \tilde{M}_{\Psi_2})$ [21].

5   Interpretation in the case of different parent particles

As another application of the effective topology method, in this section we revisit the case of *different* parent particles ($M_{A_1} \neq M_{A_2}$) as illustrated in figure 6(a). A well-motivated example of such a "coproduction" channel is provided by associated gluino-squark production which was studied in [25, 46], finding a correlation between the endpoint $M_{T2}^{\max}$ of the conventional M_{T2} variable and the larger of the two parent masses:

$$M_{T2}^{(max)}(\tilde{M}_C = M_C) = \max\left(M_{A_1}, M_{A_2}\right). \tag{5.1}$$

This result, also suggested in [12], is the analogue of eq. (1.2) for the case of different parents. Here we point out that the relation in eq. (5.1) does not hold in general. The main result in this section will be the proper interpretation of the M_{T2} kinematic endpoint in the case of different parents (figure 6(a)). The discussion will be organized as follows: in section 5.1 we first treat the case with no upstream momentum ($U_T = 0$) and then in section 5.2 we discuss the more general case with $U_T \neq 0$.

5.1   Events with no upstream momentum ($U_T = 0$)

We start from the known fact that the M_{T2} endpoint is invariant under "back-to-back" boosts in the transverse plane [17]. In the conventional case of figure 1(b) with identical parents, this boost brings both parent particles to rest. However, when the parents have different masses as in figure 6(a), no back-to-back boost can bring the parents to rest simultaneously, and the "back-to-back" boost invariance of $M_{T2}^{\max}$ will be lost. More specifically, if the parent system (A_1, A_2) is produced with some total CM energy $\sqrt{\hat{s}}$, the parent particles A_i are boosted by the respective factors

$$\eta_1\left(\sqrt{\hat{s}}\right) = \cosh^{-1}\left(\frac{\hat{s} + M_{A_1}^2 - M_{A_2}^2}{2\hat{s}\, M_{A_1}}\right), \tag{5.2}$$

$$\eta_2\left(\sqrt{\hat{s}}\right) = \cosh^{-1}\left(\frac{\hat{s} + M_{A_2}^2 - M_{A_1}^2}{2\hat{s}\, M_{A_2}}\right). \tag{5.3}$$
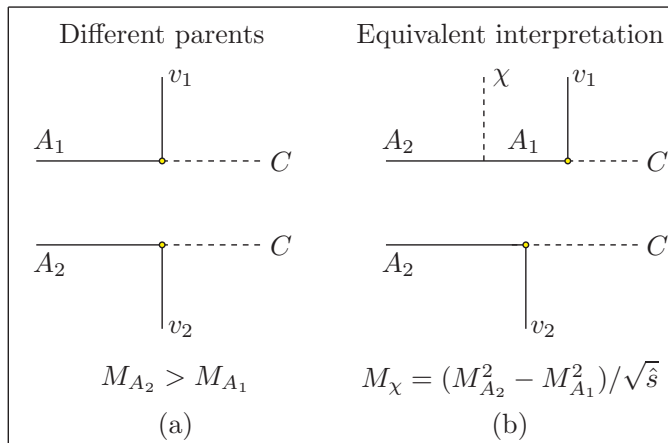
Figure 6. (a) A generic event topology with different parent particles and (b) the effective event topology for its interpretation as discussed in the text.

For definiteness and without loss of generality, from now on we shall assume that $M_{A_2} > M_{A_1}$, so that $\max(M_{A_1}, M_{A_2}) = M_{A_2}$. Then from eqs. (5.2), (5.3) it also follows that $\eta_2 < \eta_1$. Thus if we perform a "back-to-back" boost on the particles A_1 and A_2 with the boost factor η_2 corresponding to the heavier particle, the result will be that particle A_2 will be brought to rest, while the lighter parent particle A_1 will have some residual boost

$$\delta\eta(\sqrt{\hat{s}}) \equiv \eta_1(\sqrt{\hat{s}}) - \eta_2(\sqrt{\hat{s}}) = \cosh^{-1}\left[\frac{M_{A_2}^2 + M_{A_1}^2 - \left(\frac{M_{A_2}^2 - M_{A_1}^2}{\sqrt{\hat{s}}}\right)^2}{2 M_{A_2} M_{A_1}}\right]. \tag{5.4}$$

Comparing this to eq. (3.4), we see that eq. (3.4) and eq. (5.4) become identical if we identify

$$M_\chi(\sqrt{\hat{s}}) \equiv \frac{M_{A_2}^2 - M_{A_1}^2}{\sqrt{\hat{s}}}. \tag{5.5}$$

The physical meaning of eq. (5.5) is the following — the events in figure 6(a), which represent pair production of *different* parent particles, are instead reinterpreted as in figure 6(b), which shows the pair production of *identical* parents A_2, one of which decays into A_1 plus a hypothetical invisible particle χ whose mass is given by eq. (5.5). At this point it is important to note that the mass M_χ as defined in eq. (5.5) is not constant, but carries dependence on the CM energy $\sqrt{\hat{s}}$, which is inherited from eqs. (5.2), (5.3). At hadron colliders, events are produced with varying $\sqrt{\hat{s}}$, thus in general M_χ takes values in the interval

$$0 \le M_\chi(\sqrt{\hat{s}}) \le M_{A_2} - M_{A_1}, \tag{5.6}$$

where the lower bound corresponds to $\sqrt{\hat{s}} \to \infty$ and the upper bound is obtained at threshold $\sqrt{\hat{s}} = M_{A_1} + M_{A_2}$.

Once we have an event topology with equal parents as in figure 6(b), we already know how to interpret the M_{T2} endpoint — we just follow the prescription from section 3. The

topology of figure 6(b) is of the type shown in figure 2(c), so for the upper decay chain we need to introduce an effective invisible particle Ψ_1 as prescribed in figure 4(c) and eqs. (3.3), (3.4):

$$M_{\Psi_1} = M_{A_2} \left\{ 1 - \frac{M_{A_1}}{M_{A_2}} \left(1 - \frac{M_C^2}{M_{A_1}^2} \right) e^{\eta(\sqrt{\hat{s}})} \right\}, \tag{5.7}$$

$$\eta(\sqrt{\hat{s}}) = \cosh^{-1} \left\{ \frac{M_{A_2}^2 + M_{A_1}^2 - M_\chi^2(\sqrt{\hat{s}})}{2 M_{A_2} M_{A_1}} \right\} = \delta\eta(\sqrt{\hat{s}}). \tag{5.8}$$

Then, the kinematic endpoint of the usual M_{T2} variable is found from eq. (3.1):

$$M_{T2}^{\max}(\sqrt{\hat{s}}, \tilde{M}_C) = \mu(\sqrt{\hat{s}}) + \sqrt{\mu(\sqrt{\hat{s}})^2 + \tilde{M}_C^2}, \tag{5.9}$$

with $\mu(\sqrt{\hat{s}})$ given by eq. (3.8)

$$\mu(\sqrt{\hat{s}}) = e^{\eta(\sqrt{\hat{s}})/2} \cdot \frac{M_{A_2}}{2} \sqrt{\frac{M_{A_1}}{M_{A_2}} \left(1 - \frac{M_C^2}{M_{A_1}^2} \right) \left(1 - \frac{M_C^2}{M_{A_2}^2} \right)}. \tag{5.10}$$

Notice that the kinematic endpoint $M_{T2}^{\max}$ in eq. (5.9) this time depends not only on the test child mass $\tilde{M}_C$, but also on the partonic CM energy $\sqrt{\hat{s}}$. At the LHC, $\sqrt{\hat{s}}$ is not constant, but varies from one event to another in accordance with the parton distribution functions (PDFs). Therefore, the kinematic endpoint in eq. (5.9) will in general[9] get smeared. As we can see from eqs. (5.4), (5.10), $\mu(\sqrt{\hat{s}})$ is an increasing function of $\sqrt{\hat{s}}$. Since $\sqrt{\hat{s}}$ itself varies from its threshold value $\sqrt{\hat{s}} = M_{A_1} + M_{A_2}$ to $\sqrt{\hat{s}} \to \infty$, the function $\mu(\sqrt{\hat{s}})$ takes values in

$$\mu_{\min} \leq \mu(\sqrt{\hat{s}}) \leq \mu_{\max}, \tag{5.11}$$

where

$$\mu_{\min} = \lim_{\sqrt{\hat{s}} \to M_{A_1} + M_{A_2}} \mu(\sqrt{\hat{s}}) = \frac{M_{A_2}}{2} \sqrt{\frac{M_{A_1}}{M_{A_2}} \left(1 - \frac{M_C^2}{M_{A_1}^2} \right) \left(1 - \frac{M_C^2}{M_{A_2}^2} \right)}, \tag{5.12}$$

$$\mu_{\max} = \lim_{\sqrt{\hat{s}} \to \infty} \mu(\sqrt{\hat{s}}) = \frac{M_{A_2}}{2} \sqrt{\left(1 - \frac{M_C^2}{M_{A_1}^2} \right) \left(1 - \frac{M_C^2}{M_{A_2}^2} \right)} = \mu_{\min} \sqrt{\frac{M_{A_2}}{M_{A_1}}}. \tag{5.13}$$

Now it follows from eq. (5.9) that even if we choose the test mass $\tilde{M}_C$ to be the true mass M_C, the corresponding M_{T2} kinematic endpoint $M_{T2}^{\max}(M_C)$ will still vary with $\sqrt{\hat{s}}$ between a minimum value of

$$M_{T2}^{\max}(\sqrt{\hat{s}} = M_{A_1} + M_{A_2}) = \mu_{\min} + \sqrt{\mu_{\min}^2 + M_C^2} \tag{5.14}$$

and a maximum value of

$$M_{T2}^{\max}(\sqrt{\hat{s}} \to \infty) = \mu_{\max} + \sqrt{\mu_{\max}^2 + M_C^2}. \tag{5.15}$$

---

[9]Modulo the special case where A_1 and A_2 are produced in the decay of some heavy narrow resonance X as $X \to A_1 A_2$ [42, 48].
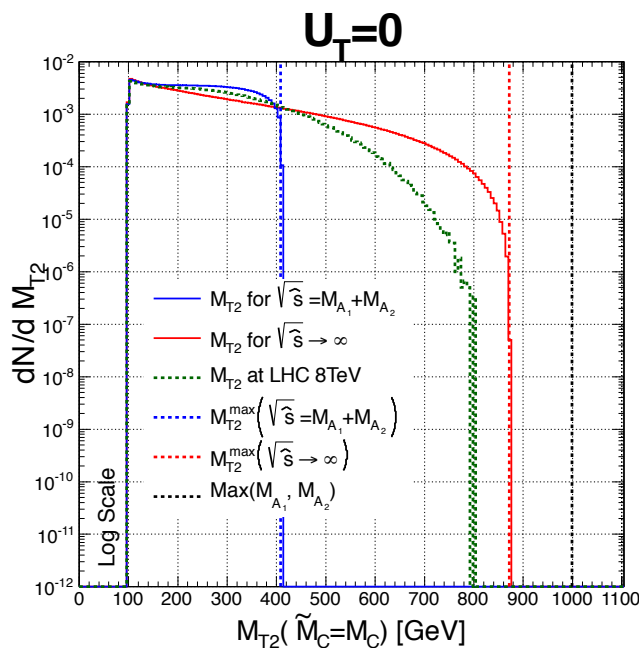
Figure 7. Unit-normalized M_{T2} distributions for the asymmetric event topology of figure 6(a) with different parent particles A_1 and A_2 and no upstream momentum ($U_T = 0$). The particle mass spectrum is chosen as $M_{A_1} = 1000\,\text{GeV}$, $M_{A_2} = 200\,\text{GeV}$ and $M_C = 100\,\text{GeV}$. The M_{T2} variable is computed with the correct value for the test mass $\tilde{M}_C = M_C = 100\,\text{GeV}$. The blue histogram uses only events at threshold ($\sqrt{\hat{s}} = M_{A_1} + M_{A_2}$) and its expected endpoint, marked by the vertical blue dashed line, is given by eq. (5.16). The red histogram shows the corresponding result in the infinite energy limit $\sqrt{\hat{s}} \to \infty$ (in practice, we take $\sqrt{\hat{s}} = 100M_{A_2}$) and the expected endpoint from eq. (5.17) is denoted by the vertical red dashed line. The black vertical dashed line is the prediction from eq. (5.1). The green dotted line is the result from Pythia 6.4 [47] simulation at LHC8 for a realistic physics example corresponding to the event topology of figure 6(a): associated squark-chargino $(\tilde{q}, \tilde{\chi}^\pm)$ production, followed by $\tilde{q} \to q + \tilde{\chi}^0$ and $\tilde{\chi}_1^\pm \to \ell^\pm + \tilde{\nu}$, for the same mass spectrum, $(M_{\tilde{q}}, M_{\tilde{\chi}^\pm}, M_{\tilde{\nu}}, M_{\tilde{\chi}^0}) = (1000, 200, 100, 100)\,\text{GeV}$.

This is illustrated in figure 7, where we plot the M_{T2} distributions for these two extreme cases: $\sqrt{\hat{s}} = M_{A_1} + M_{A_2}$ (blue) and $\sqrt{\hat{s}} \to \infty$ (red). We consider asymmetric events with different parents as in figure 6(a) and choose the mass spectrum as follows $M_{A_1} = 1000\,\text{GeV}$, $M_{A_2} = 200\,\text{GeV}$ and $M_C = 100\,\text{GeV}$. The blue and red vertical dashed lines mark the locations of the expected endpoints in eqs. (5.14) and (5.15), respectively. With the mass spectrum chosen for the figure, one gets

$$M_{T2}^{\max}(\sqrt{\hat{s}} = M_{A_1} + M_{A_2}, \tilde{M}_C = M_C) = 409.8 \text{ GeV}, \tag{5.16}$$

$$M_{T2}^{\max}(\sqrt{\hat{s}} \to \infty, \tilde{M}_C = M_C) = 873.1 \text{ GeV}. \tag{5.17}$$

figure 7 demonstrates that in these two limiting cases, the endpoints of the M_{T2} distributions agree perfectly with our expectations in eqs. (5.16), (5.17) and stay well below the conjecture of eq. (5.1), which is indicated by the black vertical dashed line.

For intermediate, more realistic values of $\sqrt{\hat{s}}$, the upper endpoints of the corresponding M_{T2} distributions will populate the region between those two extreme values, but will cer-

tainly not exceed the theoretical maximum in eq. (5.17). As an illustration, in figure 7 we also show results (the green dotted histogram) from a realistic physics example simulated with Pythia 6.4 [47]. We considered associated squark-chargino production in supersymmetry, $pp \to \tilde{q}\tilde{\chi}^{\pm}$, followed by $\tilde{q} \to q + \tilde{\chi}^0$ and $\tilde{\chi}_1^{\pm} \to \ell^{\pm} + \tilde{\nu}$, with the same mass spectrum as before, $(M_{\tilde{q}}, M_{\tilde{\chi}^{\pm}}, M_{\tilde{\nu}}, M_{\tilde{\chi}^0}) = (1000, 200, 100, 100)\,\text{GeV}$. Such events fall into the different parent category of figure 6(a). With the available statistics, the M_{T2} endpoint for the green dotted histogram happens to be around $800\,\text{GeV}$, which, as expected, is in between eq. (5.16) and eq. (5.17). We see that the realistic M_{T2} distribution indeed does not saturate the bound of eq. (5.1). Therefore, the correct interpretation of the M_{T2} endpoint in the case of different parents should be made with the help of eqs. (5.9), (5.10) instead.

5.2 Events with upstream momentum ($U_T \neq 0$)

In the previous subsection 5.1, we considered events with no upstream momentum ($U_T = 0$), where the parents A_1 and A_2 are produced back-to-back in the transverse plane. In reality, however, the inclusive (A_1, A_2) production is always associated with some amount of upstream momentum, either from initial state radiation or from decays of other, heavier particles. In this subsection we consider the effect of upstream momentum ($U_T \neq 0$) and show that our previous conclusions still hold.

It is well known that the kinematic endpoint $M_{T2}^{\max}$ in general depends on the upstream momentum U_T, but this dependence is removed for a very special choice of the test masses, namely, when the test masses are equal to the true masses of the children particles, see eq. (4.7).[10] This property has been previously demonstrated only for the case of identical parent particles and now we would like to test whether it also holds for the case of different parent particles in figure 6(a).

As we already explained, the case of different parents in figure 6(a) can be equivalently treated as a case of identical parents, which decay asymmetrically as in figure 6(b). In turn, this process can be described in terms of the asymmetric M_{T2D} variable from eq. (4.1), whose endpoint $M_{T2D}^{\max}(\tilde{M}_{\Psi_1}, \tilde{M}_{\Psi_2})$ will become independent of U_T with the following choice of test masses

$$\tilde{M}_{\Psi_1} = \frac{M_{A_2}}{M_{A_1}} M_C, \qquad \tilde{M}_{\Psi_2} = M_C. \tag{5.18}$$

These values are in principle measurable experimentally, by studying the U_T dependence of the $M_{T2D}^{\max}$ endpoint as a function of the test masses, and finding the choice where this dependence is minimized [20].

Notice that if we try to use the symmetric version of the $M_{T2}(\tilde{M}_C)$ variable, where the input masses are equal ($\tilde{M}_{C_1} = \tilde{M}_{C_2} \equiv \tilde{M}_C$), we will get a less stringent bound. Even if the test mass is taken to be the true one ($\tilde{M}_C = M_C$), we still find a chain of inequalities

$$M_{T2}^{\max}(M_C) < M_{T2D}^{\max}\left(\frac{M_{A_2}}{M_{A_1}} M_C, M_C\right) \leq M_{A_2}. \tag{5.19}$$

---

[10]The dependence on U_T completely disappears for the case of the doubly projected $M_{T2\perp}$ variable introduced in [41], which uses only the transverse momentum components orthogonal to $\vec{U}_T$.
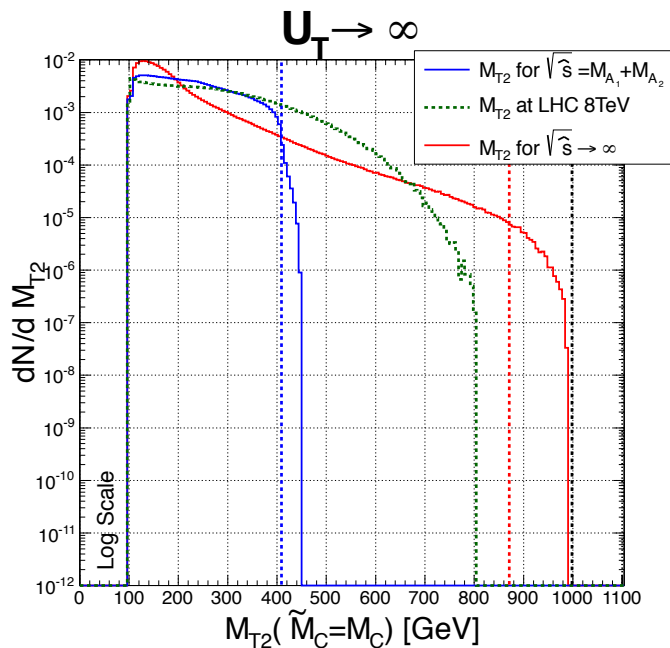
Figure 8. The same as figure 7, but for events with upstream momentum U_T. For the threshold limit ($\sqrt{\hat{s}} = M_{A_1} + M_{A_2}$) and for the infinite energy limit ($\sqrt{\hat{s}} \to \infty$), large U_T was put in by hand, while for the realistic LHC 8 TeV simulation, U_T was generated from initial state radiation in Pythia 6.4.

Of course, when the test masses $\tilde{M}_{\Psi_1}$ and $\tilde{M}_{\Psi_2}$ are chosen away from the special values in eq. (5.18), the endpoint $M_{T2D}^{\max}$ as usual will be an increasing function of U_T. The same will also be true for its symmetric counterpart $M_{T2}^{\max}$, whose U_T dependence is illustrated in figure 8, which is the analogue of figure 7 in the presence of upstream momentum U_T. As before, the vertical blue and red dashed lines mark the locations of the expected endpoints in eqs. (5.16), (5.17) in the absence of U_T. The figure shows that, as expected, in the presence of upstream momentum, the endpoints are shifted higher, and in the extreme case of infinite $\sqrt{\hat{s}}$, the endpoint eventually reaches the naive expectation from eq. (5.1):

$$\lim_{\sqrt{\hat{s}}, U_T \to \infty} M_{T2}^{\max}(\tilde{M}_C = M_C) = M_{A_2}. \tag{5.20}$$

Note that this limit is reached only in the unphysical case when both $\sqrt{\hat{s}}$ and U_T are sent to infinity. In the realistic simulation of squark-chargino production (the green dotted line), where U_T is generated from initial state radiation, the M_{T2} endpoint is similar to the one observed in figure 7 and again does not saturate the bound eq. (5.20).

5.3 Application to associated gluino-LSP production

So far we have not at all discussed the event topologies in figures 2(k) and 2(l), which can describe, e.g. associated gluino-neutralino production, where the gluino decay to the LSP gives 2 jets. Those topologies can be thought of as extreme examples of the "different parent" case just considered. Thus, $M_{T2}^{\max}$ will again depend on the center of mass energy

$\sqrt{\hat{s}}$ of the AC_2 system, which at hadron colliders will vary from one event to another. This will lead to a smearing of the endpoint $M_{T2}^{\max}$. Thus we will consider the situation where the production energy $\sqrt{\hat{s}}$ of particles A and C_2 is fixed, as at a future linear collider.

The event topology of figure 2(k). The U_T-invariant point of $M_{T2D}^{(max)}$ will appear at

$$\left(\tilde{M}_{\Psi_1}, \tilde{M}_{\Psi_2}\right) = (M_{\Psi_1}, M_{\Psi_2}),\tag{5.21}$$

where

$$M_{\Psi_1} = \frac{\sqrt{\hat{s}}}{2}\left\{1 - \frac{2M_A}{\sqrt{\hat{s}}}\left(1 - \frac{M_{B_1}^2}{M_A^2}\right)e^{\eta_s}\right\}^{1/2},\tag{5.22}$$

$$M_{\Psi_2} = \frac{\sqrt{\hat{s}}}{2}\left\{1 - \frac{2M_{B_1}}{\sqrt{\hat{s}}}\left(1 - \frac{M_{C_1}^2}{M_{B_1}^2}\right)e^{\eta_s - \eta_b}\right\}^{1/2},\tag{5.23}$$

$$\eta_s = \cosh^{-1}\left(\frac{\hat{s} + M_A^2 - M_{C_2}^2}{2\sqrt{\hat{s}}\,M_A}\right),\tag{5.24}$$

$$\eta_b = \cosh^{-1}\left(\frac{M_A^2 + M_{B_1}^2 - M_{C_1}^2}{2M_A\,M_{B_1}}\right).\tag{5.25}$$

The corresponding value of $M_{T2D}^{(max)}$ will be

$$M_{T2D}^{(max)}\left(M_{\Psi_1}, M_{\Psi_2}\right) = \frac{\sqrt{\hat{s}}}{2}.\tag{5.26}$$

The event topology of figure 2(l). With the effective topology technique, we find the U_T-invariant point at

$$\left(\tilde{M}_{\Psi_1}, \tilde{M}_{\Psi_2}\right) = (M_{\Psi}, M_{\Psi}),\tag{5.27}$$

$$M_{\Psi} = \frac{\sqrt{\hat{s}}}{2}\left\{1 - \frac{M_A}{\sqrt{\hat{s}}}\left(1 - \frac{M_{C_1}^2}{M_A^2}\right)e^{\eta_s}\right\}^{1/2},\tag{5.28}$$

with η_s still given by eq. (5.24). The endpoint is found at

$$M_{T2D}^{\max}\left(M_{\Psi}, M_{\Psi}\right) = M_{T2}^{\max}\left(M_{\Psi}\right) = \frac{\sqrt{\hat{s}}}{2}.\tag{5.29}$$

6 The shapes of $M_{T2_\perp}$ distributions

Until now we have been focusing on the measurable kinematic *endpoints* of different variables. At the same time, one could also attempt to study the *shapes* of the corresponding differential distributions. Unfortunately, (to the best of our knowledge) analytical formulas for the shapes of the M_{T2} and M_{T2D} distributions are absent. Their derivation would be rather complicated, because the shapes are affected by several factors: the production energy $\sqrt{\hat{s}}$, spin correlations, upstream momentum U_T, etc. In order to remove the U_T

effect, ref. [41] introduced a 1D-projection of M_{T2}, called $M_{T2_\perp}$. $M_{T2_\perp}$ is calculated the same way as M_{T2}, except that it uses the projections of the transverse momenta on the dimension which is orthogonal to the $\vec{U}_T$ direction [49]. It turned out that this doubly projected variable is also independent of $\sqrt{\hat{s}}$ and avoids large spin correlation effects [42]. In this section we provide analytical formulas for the shapes of the $M_{T2_\perp}$ distributions for various event topologies from figure 2. We will also discuss the endpoint behavior of these distributions, extending the technique proposed in [27] to count the number of invisible particles N_{inv}.

With two massless visible particles, $M_{T2_\perp}(\tilde{M}_\Psi)$ is related to $M_{T2_\perp}(0)$ as follows

$$x \equiv M_{T2_\perp}(0) = \frac{M_{T2_\perp}(\tilde{M}_\Psi)^2 - \tilde{M}_\Psi^2}{M_{T2_\perp}(\tilde{M}_\Psi)}. \tag{6.1}$$

The corresponding distributions are related as

$$\frac{\mathrm{d}N}{\mathrm{d}M_{T2_\perp}(\tilde{M}_\Psi)} = \left(\frac{M_{T2_\perp}(\tilde{M}_\Psi)^2 + \tilde{M}_\Psi^2}{M_{T2_\perp}(\tilde{M}_\Psi)^2} \right) \cdot \frac{\mathrm{d}N}{\mathrm{d}x} \tag{6.2}$$

Thus we only need to describe the shape of x, since the shape of $M_{T2_\perp}(\tilde{M}_\Psi)$ will then be easily obtained from eq. (6.2). In the following equations, we used the same notation for μ and η_i as in eqs. (3.2), (3.4), respectively. We also introduce individual μ_i defined as

$$\mu_i = \frac{M_A}{2} \left(1 - \frac{M_{\Psi_i}^2}{M_A^2} \right), \tag{6.3}$$

so that μ is the geometric mean of μ_1 and μ_2, as in eq. (3.2),

$$\mu = \sqrt{\mu_1 \mu_2}. \tag{6.4}$$

In the following we list our results for dN/dx.

The event topologies of figures 2(a), 2(b) and 2(e). The answer is very simple [41]

$$\frac{\mathrm{d}N}{\mathrm{d}x} \propto x \log\left(\frac{2\mu}{x} \right). \tag{6.5}$$

The event topologies of figures 2(c) and 2(f). We find

$$\frac{\mathrm{d}N}{\mathrm{d}x} \propto x \int_{\frac{x}{2\mu}}^1 \frac{\mathrm{d}p}{p} J_{\mathrm{on}}^{(1)}(p), \tag{6.6}$$

where

$$J_{\mathrm{on}}^{(i)}(p) \equiv \eta_i - \Theta\left(p - e^{-\eta_i} \right) \ln\left(p\, e^{\eta_i} \right). \tag{6.7}$$

Here $\Theta(x)$ is a unit step function and $J_{\mathrm{on}}^{(i)}(p)$ is a phase space weight from the cascade decay chain. After integrating out eq. (6.6), we get

$$\frac{\mathrm{d}N}{\mathrm{d}x} \propto x \cdot \begin{cases} 2\eta_1 \ln\left(\frac{2\mu}{x\, e^{\frac{\eta_1}{2}}} \right) & \text{if } 0 \le x < 2\mu\, e^{-\eta_1}, \\ \left[\ln\left(\frac{2\mu}{x} \right) \right]^2 & \text{if } 2\mu\, e^{-\eta_1} \le x \le 2\mu. \end{cases} \tag{6.8}$$

The event topologies of figures 2(d) and 2(g). We find

$$\frac{dN}{dx} \propto x \int_{\frac{x}{2\mu}}^{1} \frac{\mathrm{d}q}{q}\, J_{\text{off}}^{(1)}(q)\,, \tag{6.9}$$

$$J_{\text{off}}^{(i)}(q) \equiv \int_{1}^{\frac{M_A^2}{M_{\Psi_i}^2}(1-q^2)+q^2} \frac{\mathrm{d}s}{s} \sqrt{(s-1)\left(s - \frac{|M_{C_i} - M_{\chi_i}|^2}{M_{\Psi_i}^2}\right)}\,. \tag{6.10}$$

The function $J_{\text{off}}^{(i)}(q)$ is a three-body phase space weight. Integrating eq. (6.10) above, we get

$$J_{\text{off}}^{(i)}(q) = \frac{M_A^2 - M_{\Psi_i}^2}{M_{\Delta_i}^2} \sqrt{R_i - q^2}\sqrt{1-q^2} - \frac{M_{\Psi_i}}{M_{\Delta_i}} \log\left(\frac{M_{\Psi_i}\sqrt{R_i - q^2} - M_{\Delta_i}\sqrt{1-q^2}}{M_{\Psi_i}\sqrt{R_i - q^2} + M_{\Delta_i}\sqrt{1-q^2}}\right)$$
$$- \left(\frac{M_{\Psi_i}^2 + M_{\Delta_i}^2}{M_{\Delta_i}^2}\right)\left\{\frac{1}{2}\log\left(\frac{M_A^2 - M_{\Psi_i}^2}{M_{\Psi_i}^2 - M_{\Delta_i}^2}\right) + \log\left(\sqrt{R_i - q^2} + \sqrt{1-q^2}\right)\right\}, \tag{6.11}$$

with

$$M_{\Delta_i} = |M_{C_i} - M_{\chi_i}|, \quad R_i = \frac{M_A^2 - M_{\Delta_i}^2}{M_A^2 - M_{\Psi_i}^2}. \tag{6.12}$$

When χ_i is massless,

$$J_{\text{off}}^{(i)}(q) = \left(\frac{M_A^2 - M_{C_i}^2}{M_{C_i}^2}\right)(1-q^2) - \ln\left[\frac{M_A^2}{M_{C_i}^2}(1-q^2) + q^2\right], \tag{6.13}$$

and the corresponding distribution becomes

$$\frac{\mathrm{d}N}{\mathrm{d}x} \propto x\left[\frac{M_A^2 - M_{C_1}^2}{M_{C_1}^2}\left\{-1 + \frac{x^2}{4\mu^2} - 2\ln\left(\frac{x}{2\mu}\right)\right\} - 4\ln\left(\frac{M_{C_1}}{M_A}\right)\ln\left(\frac{x}{2\mu}\right)\right.$$
$$\left. + \text{Li}_2\left(\frac{2\mu_1}{M_A}\right) - \text{Li}_2\left(\frac{x^2}{2\mu_2 M_A}\right)\right], \tag{6.14}$$

where $\text{Li}_2(x)$ is Spence's function, defined as

$$\text{Li}_2(x) = -\int_0^x \mathrm{d}z \frac{\ln(|1-z|)}{z}. \tag{6.15}$$

The event topology of figure 2(h). Without loss of generality, $\eta_2 \leq \eta_1$ and we have

$$\frac{\mathrm{d}N}{\mathrm{d}x} \propto x \cdot \begin{cases} \ln\left(\frac{2\mu}{xe^{\frac{\eta_1+\eta_2}{2}}}\right) & \text{if } 0 \leq x < x_0, \\[2mm] \ln\left(\frac{2\mu}{xe^{\frac{\eta_1+\eta_2}{2}}}\right) - \frac{1}{6\eta_1\eta_2}\left[\ln\left(\frac{2\mu}{xe^{\eta_1+\eta_2}}\right)\right]^3 & \text{if } x_0 \leq x < x_1, \\[2mm] \frac{\eta_2}{6\eta_1}\left(\eta_2 - 3\ln\left(\frac{2\mu}{x}\right) + \frac{3}{\eta_2}\left[\ln\left(\frac{2\mu}{x}\right)\right]^2\right) & \text{if } x_1 \leq x < x_2, \\[2mm] \frac{1}{6\eta_1\eta_2}\left[\ln\left(\frac{2\mu}{x}\right)\right]^3 & \text{if } x_2 \leq x \leq x_3, \end{cases} \tag{6.16}$$

where

$$x_0 = 2\mu\, e^{-(\eta_1+\eta_2)}, \qquad\qquad x_1 = 2\mu\, e^{-\eta_1}, \tag{6.17}$$

$$x_2 = 2\mu\, e^{-\eta_2}, \qquad\qquad x_3 = 2\mu. \tag{6.18}$$
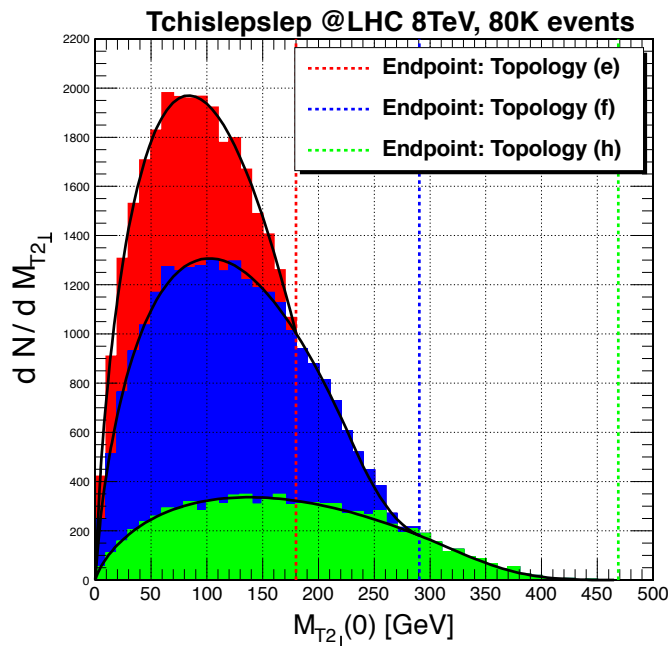
Figure 9. The same as figure 5, but for the doubly projected M_{T2} variable $M_{T2_\perp}$. The solid lines show the corresponding theoretical predictions following from eqs. (6.5), (6.8), (6.16).

The event topology of figure 2(i). We find

$$\frac{\mathrm{d}N}{\mathrm{d}x} \propto x \cdot \begin{cases} \int_{\frac{x}{2\mu}}^{\frac{xe^{\eta_1}}{2\mu}} \frac{\mathrm{d}q}{q} \ln\left(\frac{2\mu q}{x}\right) J_{\mathrm{off}}^{(2)}(q) + \int_{\frac{xe\eta_1}{2\mu}}^{1} \frac{\mathrm{d}q}{q}(\eta_1) J_{\mathrm{off}}^{(2)}(q) \ , \ \text{if } 0 \le x < x_1, \\ \int_{\frac{x}{2\mu}}^{1} \frac{\mathrm{d}q}{q} \ln\left(\frac{2\mu q}{x}\right) J_{\mathrm{off}}^{(2)}(q) \ , \ \text{if } x_1 \le x \le x_3. \end{cases} \tag{6.19}$$

The event topology of figure 2(j). We leave it in integral form

$$\frac{\mathrm{d}N}{\mathrm{d}x} \propto x \int_{\frac{x}{2\mu}}^{1} \frac{\mathrm{d}q}{q} J_{\mathrm{off}}^{(1)}(q) J_{\mathrm{off}}^{(2)}\left(\frac{x}{2\mu q}\right). \tag{6.20}$$

For illustration, in figure 9 we show the corresponding $M_{T2_\perp}$ distributions for the `Tchislepslep` SMS model considered in figure 5. In addition to the histograms which were obtained from numerical simulations, we also show the corresponding theoretical predictions following from eqs. (6.5), (6.8), (6.16). We see that the analytical results match very well the simulated $M_{T2_\perp}$ differential distributions.

As detailed in [27], it should, in principle, be possible to distinguish between topologies with different numbers of invisible particles N_{inv} simply by fitting the endpoint fall-off of kinematic distributions; this was shown to have a near-universal dependence on N_{inv} for judiciously chosen variables [27]. The near-endpoint behavior of the doubly-projected variable $M_{T2_\perp}$ for the various topologies in figure 2 is detailed in table 1 as a function of ϵ, the distance away from the endpoint. Note firstly that the fall-off for the doubly-projected variable $M_{T2_\perp}$ is faster than that for the usual stransverse mass M_{T2}. This is due to an additional dimension of the full phase space being 'projected out', and making

N_{inv}	On-shell topologies		Off-shell topologies	
	topology	near-endpoint behavior	topology	near-endpoint behavior
2	(a)	ϵ		
3	(c),(f)	ϵ^2	(d),(g)	ϵ^3
4	(h)	ϵ^3	(i)	ϵ^4
			(j)	ϵ^5

Table 1. Near-endpoint behavior of the doubly-projected stransverse mass $M_{T2\perp}$ distribution, for all topologies in figure 2, as a function of ϵ, the distance away from the endpoint. It is assumed that one invisible particle on each leg of the decay is massive (corresponding to the LSP), while any others are massless (corresponding to additional neutrinos emitted in the decay). The fall-off for alternative mass spectra can be trivially obtained by taking the relevant limit in the shape expressions given above.

it more difficult to distinguish between different numbers of invisibles N_{inv} for large N_{inv} using the endpoint behavior alone. Secondly, although the near-endpoint behavior has a universal dependence on N_{inv} for massless invisible particles [27], this is not true when any invisible particles obtain a non-negligible mass. In the latter case we see that the fall-off is always slower for true cascade decays (with on-shell resonances), since the presence of an on-shell intermediate particle effectively reduces the dimension of the full phase space, hence fewer dimensions are projected out. In fact, for cascades, the near-endpoint behavior is *entirely independent* of the invisible particle masses. Finally, note that there are discrete ambiguities between the endpoint fall-off of cascades, and decays with off-shell intermediates, for different N_{inv}. In these particular cases, then, one would need to fit using the full shape formula, given above.

7 Conclusions and summary

Our work in this paper removes some of the restrictions which so far have prevented the more widespread usage of the M_{T2} variable. We demonstrated how the M_{T2} variable (and its variants) can be usefully applied in more general situations, e.g.:

- *Decay chains with multiple invisible particles.* In sections 2 and 3 we considered cases where the new physics decay chain gives rise to *several* invisible particles. Previous M_{T2} studies have typically assumed that there is only one invisible particle in the decay chain (the dark matter WIMP), which appears at the end of the decay chain. At the same time, there are many scenarios in which *additional* invisible particles can be present. The most popular example of this sort are chargino decays in supersymmetry, which yield SM neutrinos *in addition* to the invisible LSP. We proposed two methods for dealing with the problem of additional invisibles: by introducing topology-dependent new variables (in section 2) and by reinterpreting the measured kinematic endpoints of the conventional M_{T2} distributions (in section 3).

- *Events with different invisible child particles.* In section 4 we pointed out that the reinterpretation method carries over to the case where the invisible child particles

at the end of the decay chains are different. The key idea is to use the asymmetric M_{T2D} variable introduced in [20].

- *Events with different parent particles.* Much of the previous literature on M_{T2} dealt only with events in which the two parent particles initiating the decay chains are identical. As for events with different parent particles, it was thought that the M_{T2} endpoint in that case reveals the mass of the *heavier* parent. In section 5 we showed that this conjecture is false, and we gave the correct interpretation of the M_{T2} endpoint for the case of different parent particles.

Apart from a good theoretical understanding of the measured M_{T2} endpoint in terms of the underlying mass spectrum in all those different situations, it is also important to have a good knowledge of the shapes of the respective differential M_{T2} distributions. In section 6 we considered the doubly projected variable $M_{T2\perp}$ proposed in [41] and derived the corresponding shapes for a number of different cases shown in figure 2(a-j). Our formulas can be used for improving the precision of mass measurements based on $M_{T2\perp}$ kinematic endpoints [8]. Furthermore, by comparing the different shape predictions to the data, one could also, in principle, deduce the correct event topology and/or the number of invisible particles in the event, although in practice this may be unfeasible due to limited statistics near the endpoint.

Acknowledgments

A   Derivation of the effective particle mass

In this section, we derive the formula (3.3) for the effective mass M_{Ψ_i} for the case of the decay chain in figure 4(c). The main idea is to investigate the allowed range for the transverse momentum P_{vT} of the visible particle v (it will be convenient to do this analysis in the rest frame of particle A).

Starting in the rest frame of B, the allowed range for P_{vT} is given by

$$0 \le P_{vT}^{(B)} \le \frac{M_B}{2} \left(1 - \frac{M_C^2}{M_B^2} \right), \tag{A.1}$$

where the superscript (B) denotes that the momentum is measured in the B rest frame.

Next, the rest frame of B is related to the rest frame of A by a Lorentz boost along the direction of the momentum of B in the A rest frame, $\vec{P}_B^{(A)}$:

$$\begin{pmatrix} \cosh\eta & \sinh\eta \\ \sinh\eta & \cosh\eta \end{pmatrix} \begin{pmatrix} M_B \\ 0 \end{pmatrix} = \begin{pmatrix} E_B^{(A)} \\ P_B^{(A)} \end{pmatrix}, \tag{A.2}$$

where $E_B^{(A)}$ and $P_B^{(A)}$ are respectively the energy and the magnitude of the momentum of B in the A rest frame:

$$E_B^{(A)} = \frac{M_A^2 + M_B^2 - M_\chi^2}{2M_A}, \tag{A.3}$$

$$P_B^{(A)} = \frac{\sqrt{\left(M_A^2 - (M_B + M_\chi)^2\right)\left(M_A^2 - (M_B - M_\chi)^2\right)}}{2M_B}. \tag{A.4}$$

Given the Lorentz boost factor η, the allowed range for the transverse momentum $P_{vT}^{(A)}$ of v in the A rest frame is

$$0 \leq P_{vT}^{(A)} \leq \frac{M_B}{2}\left(1 - \frac{M_C^2}{M_B^2}\right)(\cosh\eta + \sinh\eta) = \frac{M_B}{2}\left(1 - \frac{M_C^2}{M_B^2}\right)e^\eta, \tag{A.5}$$

where η is found from (A.2):

$$\eta = \cosh^{-1}\left(\frac{M_A^2 + M_B^2 - M_\chi^2}{2M_A M_B}\right), \tag{A.6}$$

which was already shown in (3.4). Now, we are ready to present the equivalent diagram of figure 4(e), in which particle A decays into v and Ψ so that the allowed range of the transverse momentum of v for the equivalent diagram is the same as the range found in (A.5). For a generic two-body decay $A \to v + \Psi$, the allowed range of the transverse momentum $P_{vT}^{(A)}$ of v is

$$0 \leq P_{vT}^{(A)} \leq \frac{M_A}{2}\left(1 - \frac{M_\Psi^2}{M_A^2}\right), \tag{A.7}$$

where M_Ψ is the mass of the effective particle Ψ. Now, by comparing (A.7) and (A.5), we obtain the desired value of M_Ψ:

$$M_\Psi(M_A, M_B, M_C, M_\chi) = M_A\left\{1 - \frac{M_B}{M_A}\left(1 - \frac{M_C^2}{M_B^2}\right)e^\eta\right\}^{1/2}, \tag{A.8}$$

which was the result shown in (3.3).

Open Access. This article is distributed under the terms of the Creative Commons Attribution License which permits any use, distribution and reproduction in any medium, provided the original author(s) and source are credited.

References

[1] A.J. Barr and C.G. Lester, *A Review of the Mass Measurement Techniques proposed for the Large Hadron Collider*, *J. Phys.* **G 37** (2010) 123001 [arXiv:1004.2732] [INSPIRE].

[2] A. Barr et al., *Guide to transverse projections and mass-constraining variables*, *Phys. Rev.* **D 84** (2011) 095031 [arXiv:1105.2977] [INSPIRE].

[3] C. Lester and D. Summers, *Measuring masses of semiinvisibly decaying particles pair produced at hadron colliders*, *Phys. Lett.* **B 463** (1999) 99 [hep-ph/9906349] [INSPIRE].

[4] A. Barr, C. Lester and P. Stephens, m_{T2}: the Truth behind the glamour, J. Phys. **G 29** (2003) 2343 [hep-ph/0304226] [INSPIRE].

[5] CDF collaboration, T. Aaltonen et al., Top Quark Mass Measurement using m_{T2} in the Dilepton Channel at CDF, Phys. Rev. **D 81** (2010) 031102 [arXiv:0911.2956] [INSPIRE].

[6] ATLAS collaboration, Search for squarks and gluinos using final states with jets and missing transverse momentum with the ATLAS detector in $\sqrt{s} = 7$ TeV proton-proton collisions, Phys. Lett. **B 701** (2011) 186 [arXiv:1102.5290] [INSPIRE].

[7] CMS collaboration, Search for supersymmetry in hadronic final states using M_{T2} in pp collisions at $\sqrt{s} = 7$ TeV, JHEP **10** (2012) 018 [arXiv:1207.1798] [INSPIRE].

[8] CMS collaboration, Mass determination in the $t\bar{t}$ system with kinematic endpoints, CMS-PAS-TOP-11-027.

[9] D0 collaboration, V.M. Abazov et al., Search for Higgs boson production in oppositely charged dilepton and missing energy events in $p\bar{p}$ collisions at $\sqrt{s} = 1.96$ TeV, Phys. Rev. **D 86** (2012) 032010 [arXiv:1207.1041] [INSPIRE].

[10] A. Barr, Measuring slepton spin at the LHC, JHEP **02** (2006) 042 [hep-ph/0511115] [INSPIRE].

[11] L. Randall and D. Tucker-Smith, Dijet Searches for Supersymmetry at the LHC, Phys. Rev. Lett. **101** (2008) 221803 [arXiv:0806.1049] [INSPIRE].

[12] A.J. Barr and C. Gwenlan, The Race for supersymmetry: using m_{T2} for discovery, Phys. Rev. **D 80** (2009) 074007 [arXiv:0907.2713] [INSPIRE].

[13] M.M. Nojiri and J. Shu, Two jets and missing E_T signature to determine the spins of the new particles, JHEP **06** (2011) 047 [arXiv:1101.2701] [INSPIRE].

[14] K.T. Matchev, F. Moortgat, L. Pape and M. Park, Precision sparticle spectroscopy in the inclusive same-sign dilepton channel at LHC, Phys. Rev. **D 82** (2010) 077701 [arXiv:0909.4300] [INSPIRE].

[15] G. Bélanger, S. Kraml and A. Lessa, Light Sneutrino Dark Matter at the LHC, JHEP **07** (2011) 083 [arXiv:1105.4878] [INSPIRE].

[16] W.S. Cho, K. Choi, Y.G. Kim and C.B. Park, Gluino Stransverse Mass, Phys. Rev. Lett. **100** (2008) 171801 [arXiv:0709.0288] [INSPIRE].

[17] W.S. Cho, K. Choi, Y.G. Kim and C.B. Park, Measuring superparticle masses at hadron collider using the transverse mass kink, JHEP **02** (2008) 035 [arXiv:0711.4526] [INSPIRE].

[18] A.J. Barr, B. Gripaios and C.G. Lester, Weighing Wimps with Kinks at Colliders: Invisible Particle Mass Measurements from Endpoints, JHEP **02** (2008) 014 [arXiv:0711.4008] [INSPIRE].

[19] M. Burns, K. Kong, K.T. Matchev and M. Park, Using Subsystem M_{T2} for Complete Mass Determinations in Decay Chains with Missing Energy at Hadron Colliders, JHEP **03** (2009) 143 [arXiv:0810.5576] [INSPIRE].

[20] P. Konar, K. Kong, K.T. Matchev and M. Park, Dark Matter Particle Spectroscopy at the LHC: Generalizing M_{T2} to Asymmetric Event Topologies, JHEP **04** (2010) 086 [arXiv:0911.4126] [INSPIRE].

[21] A.J. Barr, B. Gripaios and C.G. Lester, Transverse masses and kinematic constraints: from the boundary to the crease, JHEP **11** (2009) 096 [arXiv:0908.3779] [INSPIRE].

[22] A.J. Barr and C.G. Lester, *Oxbridge stransverse mass library*,
http://www.hep.phy.cam.ac.uk/%7Elester/mt2/index.html

[23] H.-C. Cheng and Z. Han, *Minimal Kinematic Constraints and m_{T2}*, *JHEP* **12** (2008) 063
[http://particle.physics.ucdavis.edu/hefti/projects/doku.php?id=wimpmass]
[arXiv:0810.5178] [INSPIRE].

[24] Y. Bai, H.-C. Cheng, J. Gallicchio and J. Gu, *Stop the Top Background of the Stop Search*,
JHEP **07** (2012) 110 [arXiv:1203.4813] [INSPIRE].

[25] M.M. Nojiri, K. Sakurai, Y. Shimizu and M. Takeuchi, *Handling jets + missing E(T)
channel using inclusive m_{T2}*, *JHEP* **10** (2008) 100 [arXiv:0808.1094] [INSPIRE].

[26] K. Agashe, D. Kim, D.G. Walker and L. Zhu, *Using M_{T2} to Distinguish Dark Matter
Stabilization Symmetries*, *Phys. Rev.* **D 84** (2011) 055020 [arXiv:1012.4460] [INSPIRE].

[27] G.F. Giudice, B. Gripaios and R. Mahbubani, *Counting dark matter particles in LHC events*,
Phys. Rev. **D 85** (2012) 075019 [arXiv:1108.1800] [INSPIRE].

[28] M. Blanke, D. Curtin and M. Perelstein, *SUSY-Yukawa Sum Rule at the LHC*, *Phys. Rev.* **D
82** (2010) 035020 [arXiv:1004.5350] [INSPIRE].

[29] A. Rajaraman and F. Yu, *A New Method for Resolving Combinatorial Ambiguities at Hadron
Colliders*, *Phys. Lett.* **B 700** (2011) 126 [arXiv:1009.2751] [INSPIRE].

[30] Y. Bai and H.-C. Cheng, *Identifying Dark Matter Event Topologies at the LHC*, *JHEP* **06**
(2011) 021 [arXiv:1012.1863] [INSPIRE].

[31] P. Baringer, K. Kong, M. McCaskey and D. Noonan, *Revisiting Combinatorial Ambiguities
at Hadron Colliders with M_{T2}*, *JHEP* **10** (2011) 101 [arXiv:1109.1563] [INSPIRE].

[32] K. Choi, D. Guadagnoli and C.B. Park, *Reducing combinatorial uncertainties: A new
technique based on M_{T2} variables*, *JHEP* **11** (2011) 117 [arXiv:1109.2201] [INSPIRE].

[33] W.S. Cho, D. Kim, K.T. Matchev and M. Park, *Cracking the dark matter code at the LHC*,
arXiv:1206.1546 [INSPIRE].

[34] G.G. Ross and M. Serna, *Mass determination of new states at hadron colliders*, *Phys. Lett.*
B 665 (2008) 212 [arXiv:0712.0943] [INSPIRE].

[35] A.J. Barr, A. Pinder and M. Serna, *Precision Determination of Invisible-Particle Masses at
the CERN LHC. II.*, *Phys. Rev.* **D 79** (2009) 074005 [arXiv:0811.2138] [INSPIRE].

[36] B. Webber, *Mass determination in sequential particle decay chains*, *JHEP* **09** (2009) 124
[arXiv:0907.5307] [INSPIRE].

[37] L. Harland-Lang, C. Kom, K. Sakurai and W. Stirling, *Measuring the masses of a pair of
semi-invisibly decaying particles in central exclusive production with forward proton tagging*,
Eur. Phys. J. **C 72** (2012) 1969 [arXiv:1110.4320] [INSPIRE].

[38] L. Harland-Lang, C. Kom, K. Sakurai and W. Stirling, *Mass Shell Technique for Measuring
Masses of a Pair of Semi-Invisibly Decaying Particles*, *Phys. Rev. Lett.* **108** (2012) 181805
[arXiv:1202.0047] [INSPIRE].

[39] G. Polesello and D.R. Tovey, *Supersymmetric particle mass measurement with the
boost-corrected contransverse mass*, *JHEP* **03** (2010) 030 [arXiv:0910.0174] [INSPIRE].

[40] D.R. Tovey, *On measuring the masses of pair-produced semi-invisibly decaying particles at
hadron colliders*, *JHEP* **04** (2008) 034 [arXiv:0802.2879] [INSPIRE].

[41] P. Konar, K. Kong, K.T. Matchev and M. Park, *Superpartner Mass Measurement Technique using* 1*D Orthogonal Decompositions of the Cambridge Transverse Mass Variable* M_{T2}, *Phys. Rev. Lett.* **105** (2010) 051802 [arXiv:0910.3679] [INSPIRE].

[42] L. Edelhauser, K.T. Matchev and M. Park, *Spin effects in the antler event topology at hadron colliders*, *JHEP* **11** (2012) 006 [arXiv:1205.2054] [INSPIRE].

[43] P. Konar, K. Kong and K.T. Matchev, $\sqrt{\hat{s}}_{min}$: *A Global inclusive variable for determining the mass scale of new physics in events with missing energy at hadron colliders*, *JHEP* **03** (2009) 085 [arXiv:0812.1042] [INSPIRE].

[44] P. Konar, K. Kong, K.T. Matchev and M. Park, *RECO level* $\sqrt{s}_{\min}$ *and subsystem* $\sqrt{s}_{\min}$: *improved global inclusive variables for measuring the new physics mass scale in* $/\!\!\!E_T$ *events at hadron colliders*, *JHEP* **06** (2011) 041 [arXiv:1006.0653] [INSPIRE].

[45] CMS Collaboration, *Interpretation of Searches for Supersymmetry*, CMS-PAS-SUS-11-016.

[46] M.M. Nojiri, Y. Shimizu, S. Okada and K. Kawagoe, *Inclusive transverse mass analysis for squark and gluino mass determination*, *JHEP* **06** (2008) 035 [arXiv:0802.2412] [INSPIRE].

[47] T. Sjöstrand, S. Mrenna and P.Z. Skands, *PYTHIA 6.4 Physics and Manual*, *JHEP* **05** (2006) 026 [hep-ph/0603175] [INSPIRE].

[48] T. Han, I.-W. Kim and J. Song, *Kinematic Cusps: Determining the Missing Particle Mass at Colliders*, *Phys. Lett.* **B 693** (2010) 575 [arXiv:0906.5009] [INSPIRE].

[49] K.T. Matchev and M. Park, *A General method for determining the masses of semi-invisibly decaying particles at hadron colliders*, *Phys. Rev. Lett.* **107** (2011) 061801 [arXiv:0910.1584] [INSPIRE].